JACS
JOURNAL OF THE AMERICAN CHEMICAL SOCIETY

Article

pubs.acs.org/JACS

Bioluminescence of Firefly Squid via Mechanism of Single Electron-Transfer Oxygenation and Charge-Transfer-Induced Luminescence

Bo-Wen Ding and Ya-Jun Liu*

Key Laboratory of Theoretical and Computational Photochemistry, Ministry of Education, College of Chemistry, Beijing Normal University, Beijing 100875, China

Supporting Information

ABSTRACT: *Watasenia scintillans* (*W. scintillans*) is a deep-sea luminescent squid with a popular name of firefly squid. It produces flashes of blue light via a series of complicated luciferin-luciferase reactions involving ATP, Mg^{2+}, and molecular oxygen. Tsuji has proposed a hypothetical scheme for this mysterious bioluminescence (BL) process, but the proposal is short of strong evidence experimentally or theoretically, especially for two key steps. They are the addition of molecular oxygen to luciferin and the formation of light emitter. For the first time, the present study investigates the two steps by reliable density functional theory (DFT) and time-dependent DFT. The results of calculated energetics, charge transfer process, electronic structures, and molecular dynamics give convincing support for Tsuji's proposal. The oxygenation reaction occurs with a single electron-transfer (SET) mechanism, and the light emitter is produced via the mechanism of gradually reversible charge-transfer-induced luminescence (GRCTIL). The simulation of nonadiabatic molecular dynamics further confirms the GRCTIL mechanisms and evaluates the quantum yield of the light emitter to be 43%. The knowledge obtained in the current study will help to understand a large amount of BL systems in nature, since the core structure of *W. scintillans* luciferin, imidazopyrazinone, is common in the luciferins of about eight phyla of luminescent organisms.

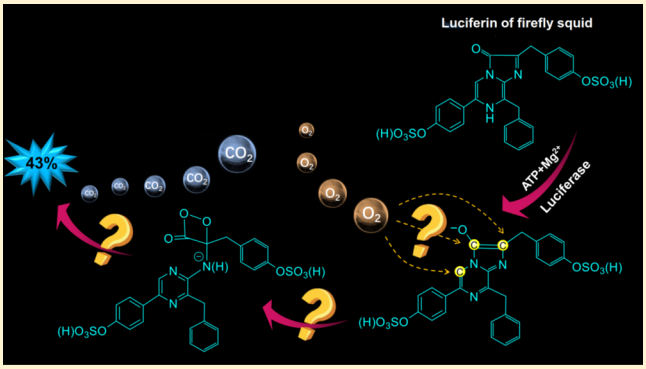

1. INTRODUCTION

Bioluminescence (BL) is an amazing phenomenon produced by a living organism. It has received extensive attention as a subject of life science and a powerful analytical tool in medical applications, such as noninvasive real-time imaging for target molecules in vivo.[1−3] There are more than 700 genera known to produce BL, and within them the most famous one could be the firefly.[4] Some other terrestrial creatures are also able to produce BL, such as fungi[5] and earthworms.[6] Nevertheless, about 80% of luminous organisms live in the ocean from bacteria to fish.[7,8] *Watasenia scintillans* (*W. scintillans*) is a luminescent squid living in the deep sea.[9] It has ∼6 cm mantle length and is almost entirely covered by thousands of photophores that emit light in synchronous or nonsynchronous pattern.[10] *W. scintillans* produces bright blue flashes (470 nm) like the firefly from its tips of arms,[11] so it is popularly called firefly squid. Firefly squids glow brilliantly off the coast when they gather in millions during spawning period.[12] How is the glamorous light produced? Generally speaking, luminous squid emits light in three ways.[9] One, the light is emitted by symbiotic luminous bacteria harboring in its photophores, such as Hawaiian bobtail squid (*Euprymna scolopes*) that produces light by symbiotic bacteria (*Vibrio fischeri*).[13−16] Two, luminous mucus instead of ink is ejected from the luminous organ of squid into the sea. This kind of BL is common in deep-sea squid, such as *Heteroteuthis dispar*.[17] Three, the most common way for BL creatures is when the light is emitted by endocellular chemiluminescent reactions in photoprotein or luciferin-luciferase system. In the former case, a photoprotein is first formed, then the BL is produced after the photoprotein encounters some necessary chemicals. For instance, *Symplectoteuthis oualaniensis* emits light in the presence of oxygen molecule and metal cations (such as Na^+ and K^+) after dehydrocoelenterazine (Chart 1A) links to a protein at a cysteine residue to form the photoprotein (symplectin, Chart 1B).[18−23] In the latter case, the luciferase catalyzes the oxidation of luciferin to produce the light emitter. The BL of *W. scintillans* is a typical example of the latter case.[10,11] The light is produced via an ATP-dependent luciferin-luciferase reaction (the optimal pH value of 8.8) involving oxygen molecule and Mg^{2+}.[9] The luciferin of *W. scintillans* is a disulfonate derivative of coelenterazine (Chart 1C), i.e., coelenterazine disulfonate (Chart 1D), which has been isolated from the photophores of *W. scintillans*.[24−26] Although coelenterazine was isolated in the liver of *W. scintillans*, coelenterazine disulfonate was not isolated in liver but in arm photophores under complete exclusion of oxygen, which gave

Received: August 31, 2016
Published: December 29, 2016

DOI: 10.1021/jacs.6b09119
J. Am. Chem. Soc. 2017, 139, 1106−1119

Chart 1[a]

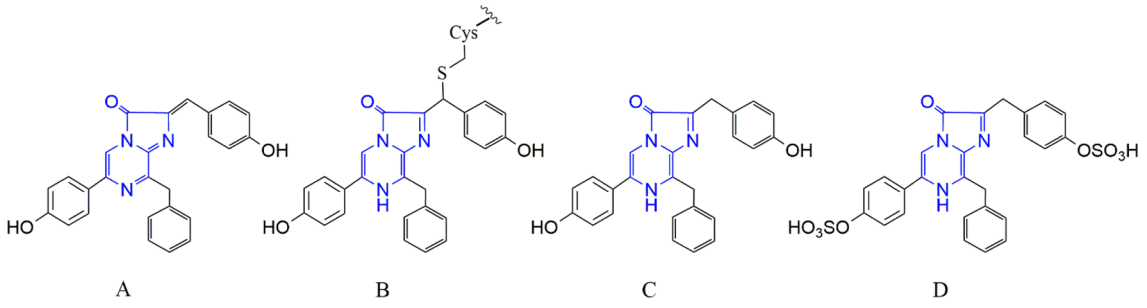

[a]A is dehydrocoelenterazine, B is the photoprotein for *S. oualaniensis* BL (symplectin), C is coelenterazine, and D is the luciferin of *W. scintillans* (coelenterazine disulfonate), where the skeleton in blue (**ImPy**) is the common core of many luminescent substrates.

Scheme 1. A Postulated Mechanism of *W. scintillans* BL Reported in Ref 11

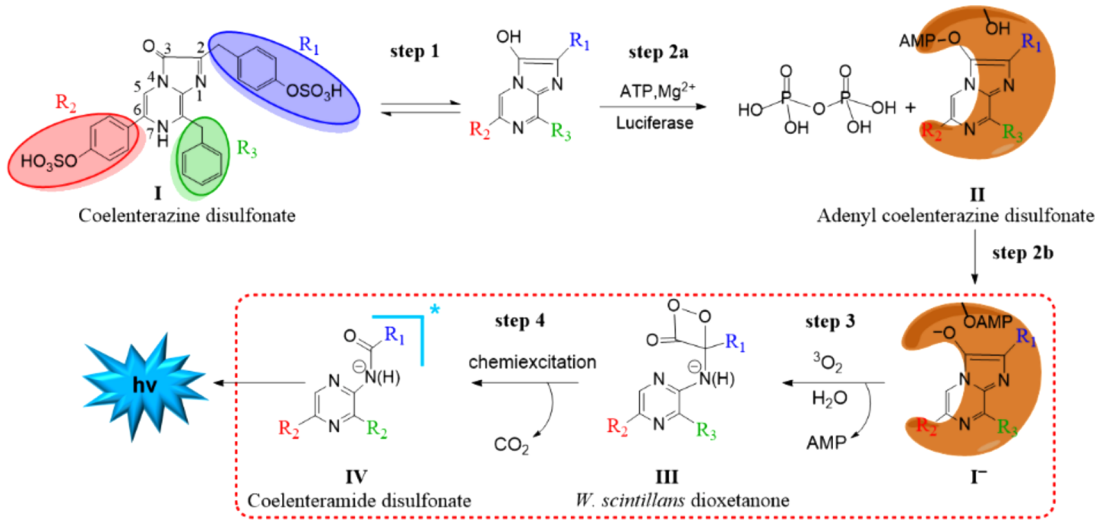

Scheme 2. $^3O_2$ Addition Paths for ImPys at Three (C_2-, C_3-, or C_5-) Possible Positions

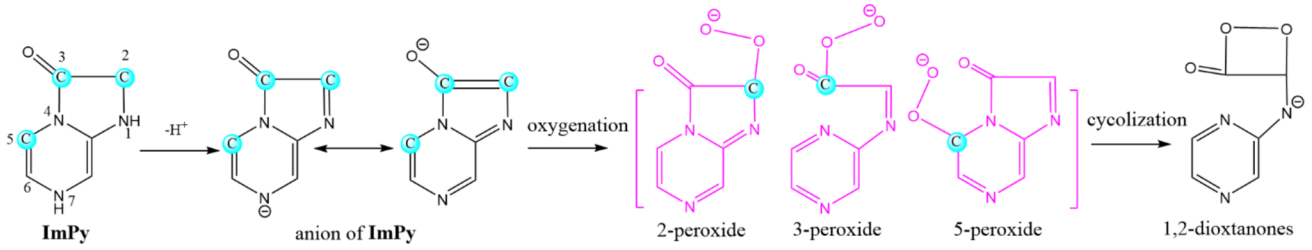

strong chemiluminescence (CL) in aqueous cellosolve. So coelenterazine disulfonate was identified as the luciferin of *W. scintillans*.[26] Coelenterazine disulfonate has an imidazopyrazinone skeleton (**ImPy**) (blue part in Chart 1). Besides the firefly and bacteria BL, the BL coming from **ImPy** derivatives (**ImPys**) based luciferin or luminescent substrate of photoprotein is the most known one, which covers eight phyla (radiolaria, cnidaria, chordata, ctenophora, mollusca, arthropoda, echinodermata, chaetognatha).[8,27,28] Analyzing the BL process is helpful to understand the corresponding bioluminescent mechanism and provides theoretical reference on biotechnology and biomedical applications.

Tsuji has proposed a possible reaction process for the BL of *W. scintillans* as shown in Scheme 1.[11] Step 1, a rapid enolization of the keto oxygen on C_3 of *W. scintillans* luciferin (**I**) takes place accompanying with the departure of H from N_7. Step 2a, the enol group of **I** is adenylated by ATP under the catalysis of luciferase (Mg^{2+} as the cofactor) to form adenyl coelenterazine disulfonate (**II**). Step 2b, the AMP group is removed from **II** along with the formation of the anionic form of **I** (I^-). Step 3, the oxygenation of I^- generates a dioxetanone intermediate (**III**). Step 4, due to low stability, **III** decomposes to coelenteramide disulfonate (**IV**) and CO_2 along with the emission of blue light. But until now, there has not been any strong theoretical or experimental evidence to support Tsuji's proposal. The four main problems are (1) whether ADP or AMP is produced in the adenylation of **I**;[29] (2) the detailed mechanisms for oxygenation of I^- by $^3O_2$ (step 3 shown in red box) is uncovered; (3) the decomposition process of **III** (step 4) is unclear; (4) the exact chemical form of light emitter is not identified. The last two steps in the proposed bioluminescent process are responsible for producing light emitter. Compre-

DOI: 10.1021/jacs.6b09119
J. Am. Chem. Soc. 2017, 139, 1106−1119

hension to the oxygenation and decomposition in steps 3 and 4, respectively, is the key to understand the *W. scintillans* BL.

The oxygenation process is not only crucial to *W. scintillans* BL, but also a general step in almost all oxygen-dependent BL systems, such as firefly,[30] sea firefly,[31] jellyfish,[32] *Obelia*,[33] and bacteria.[34] For the oxygenation of $\mathbf{I}^-$, as summarized in Scheme 2, the oxygen molecule may attack the **ImPy** skeleton in $\mathbf{I}^-$ at three possible positions, C_2,[35−41] C_3,[42,43] or C_5[44,45] to form 2-, 3-, or 5-peroxide anion adduct, respectively. Which is the most likely position? Besides, there are two possible pathways when $^3O_2$ attacks $\mathbf{I}^-$, i.e., a direct attacking way without single electron transfer (SET) and a radical-based pathway with SET from $\mathbf{I}^-$ to $^3O_2$ via $O_2^{\bullet-}$.[46] Which one is more feasible? $\mathbf{I}^-$ is a derivative of **ImPy** as shown in Chart 1. Although oxygenation of $\mathbf{I}^-$ itself has not been investigated, the possible positions of oxygenation of some other **ImPy**s were previously studied by several groups.[41,46−51] Branchini et al. detected the presence of superoxide anion in the chemical model reaction of firefly BL, and pointed out that firefly BL is initiated by a SET from firefly luciferin to molecule oxygen.[52] The SET-oxygenation mechanism has been proposed for the coelenterazine BL reaction.[49,53]

The core structure in **III** is the four-membered ring (1,2-dioxetanone), which is important not only for *W. scintillans* BL, but for the BL of firefly,[30] seafirefly,[31] jellyfish,[32,54] *Obelia*,[50,53,55,56] earthworm,[6] *Latia*,[57] and the CL of luminol,[58] AMPPD,[59] acridinium ester,[60] and so on. The derivatives of 1,2-dioxetanone (dioxetanones) have been researched extensively and assumed to decompose with two kinds of forms, neutral and anionic. Our previous studies have concluded for several dioxetanes[61] or dioxetanones.[30,31,59,62−64] The thermolysis of their neutral form follows the two-step biradical (entropic trapping) mechanism,[30,31,61−64] where the C−C′ bond cleaves after the complete breakage of O−O′ bond. The decomposition process involves two transition states (TSs) and one biradical intermediate. In contrast to the negligible charge transfer (CT) in the decomposition of the neutral dioxetanones/dioxetanes, the decomposition of the anionic ones is induced by an obvious CT. It abides by the gradually reversible charge-transfer-induced luminescence (GRCTIL) mechanism.[30] In the GRCTIL mechanism, the CT and back CT (BCT) occur gradually concerted with the ruptures of O−O′ and C−C′ bonds, respectively. The "double crossing" between the potential energy surfaces (PESs) of the ground (S_0) and the first singlet (S_1) states is responsible for producing the light emitter.

Herein, the detailed processes and mechanisms of the **I** oxygenation and the **III** decomposition were thoroughly investigated by means of reliable density functional theory (DFT) and time-dependent DFT (TDDFT). The decomposition of **III** was also simulated by nonadiabatic molecular dynamics approach and the quantum yield of chemiexcitation was estimated. The knowledge obtained from *W. scintillans* BL in the current study could be expanded to a large area, because the core structure, **ImPy** skeleton in $\mathbf{I}^-$ is universal in the luciferin of about eight phyla of bioluminescent organisms.

2. COMPUTATIONAL DETAILS

Although the 3- and 5-peroxide intermediates were not detected in experimental investigations for the oxygenation of **ImPy**s,[47] the C_3-oxygenation could not be ruled out rashly. Because the dioxetanone intermediate can be formed directly in one-step reaction instead of through a 3-peroxide intermediate, but not be directly produced by C_5-oxygenation without any intermediates (Scheme 2). The detailed processes of C_2- and C_3-oxygenation of **I** were considered in this study. The reactant model is the trianion state of **I** ($\mathbf{I}^{3-}$), whose amide on N_7 and two sulfonic group were all deprotonated, since the benzenesulfonic acid is a strong one. (The oxygenation of the monoanion state of **I** ($\mathbf{I}^-$) with protonated sulfonic group ($-OSO_3H$) were also computed and the mechanism showed no obvious differences from the one of $\mathbf{I}^{3-}$. (see Supporting Information (SI)) The equilibrium geometries of reactant complex (RC) formed by the **I** and superoxide anion radicals as starting reacting point TS, intermediate (Int), and product on the S_0-state surface were fully optimized with the Coulomb-attenuated hybrid exchange-correlation functional (CAM-B3LYP)[65] in DMSO with polarizable continuum model (PCM). For currently targeted systems, adding dispersion correction to CAM-B3LYP does not much change the calculated results (see SI). The unrestricted open-shell approximation was used to treat triplet- and singlet-state biradical species, in which the broken-symmetry technique was introduced to treat singlet-state biradical. The calculations of harmonic frequency, zero-point vibrational energy (ZVE), and thermodynamics data were carried out at the same theoretical level as the corresponding optimization. The intrinsic reaction coordinates (IRC) was performed to ensure that each TS connects the correct reactant and product. Mulliken population analysis was carried out to observe the variations of charge populations along the reaction path. The ET rate (k_{ET}) was estimated based on Marcus theory[66] (the computational method is detailedly described in SI).

For the decomposition of **III**, the protonated ($\mathbf{III}^{2-}$-H) and deprotonated ($\mathbf{III}^{3-}$) forms of amide on N_1 atom with two $-OSO_3^-$ were used as the reactant models. All the electronic structure computations including geometric optimizations, vibrational frequency analyses for stationary points, and IRC on the S_0-state surface were carried out in gas phase at the same theoretical levels as did in the oxygenation of $\mathbf{I}^{3-}$. The Mulliken population analysis was performed to identify any possible CT characteristics. The linear response time-dependent density functional theory (LR-TDDFT) was used to obtain the energies and transition properties of the S_1 state based on the optimized geometric structure on the S_0-state PES. This method has been proved to be able to qualitatively describe the decomposition of dioxetanones.[30,31,62] For comparison, the decomposition processes of another two forms (**III** and $\mathbf{III}^-$ with $-OSO_3H$) of the *W. scintillans* dioxetanone were also investigated by the same methods (see SI for detailed computational results). The chemiluminescent decomposition of **III** was also simulated by the on-the-fly trajectory surface hopping (TSH) dynamics in the framework of Tully's fewest approach. In the TSH simulation, SF-DFT[67−69] was used to calculate the potential energies of the S_0 and S_1 states, and nuclear gradients, which incorporates the spin-flip (SF) scheme and the Tamm/Dancoff approximation (TDA)[70−72] to TDDFT. It performs well in describing open-shell systems than the conventional Kohn−Sham DFT and giving the correct topology of S_0/S_1 CI.[73,74] The BHHLYP functional was selected in the SF-DFT calculation, the results of which have been compared with that of (TD) CAM-B3LYP and the second-order multiconfiguration perturbation theory (CASPT2) levels on firefly dioxetanone anion.[75] The nonadiabatic couplings between different electronic states were derived by numerically differentials of the wave function overlaps between two successive time steps with a small duration.[76,77] The Newton equations were integrated using the velocity Verlet algorithm[78−80] with a constant time step of 0.5 fs and a maximum simulation time of 100 fs. In the initial samplings, random velocities at a constant temperature of 300 K and at a fixed TS geometry were sampled as initial condition, according to the algorithm proposed by Sellner et al.[81] Thus, the statistical behaviors of trajectories can be described by the canonical ensemble (NVT). The ZVE of TS (11.5 eV of $\mathbf{III}^{3-}$, 12.1 eV for $\mathbf{III}^-$) was chosen as the initial kinetic energy. The above nonadiabatic molecular dynamics approach was also adopted to estimate the quantum yield of the light emitter (the quantum yield of chemiexcitation, Φ_S) in the thermolysis of $\mathbf{III}^{3-}$ and $\mathbf{III}^-$. This approach has been successfully employed to the chemiluminescent decomposition of firefly dioxetanone anion.[30] Φ_S is also estimated based on Landau−Zener formula (see details in the

DOI: 10.1021/jacs.6b09119
J. Am. Chem. Soc. 2017, 139, 1106−1119

SI).[82−84] The solvent effect of $\mathbf{III}^{2-}$ and $\mathbf{III}^{3-}$ in DMSO were considered with PCM model. The 6-31G(d,p) basis set[85,86] was employed in all of the electronic structure computations and dynamics simulations, since our previous studies have indicated that the larger basis sets (6-31+G(d,p) and 6-31++G(d,p)), do not improve the calculated results.[30]

The DFT and LR-TDDFT computations were performed using the Gaussian 09[87] program suite. The TSH simulations were performed by Newton-X program package[88,89] with the electronic energies and nuclear gradients computed by the SF-DFT method in GAMESS-US.[90] The interface connects Newton-X and GAMESS for TSH simulation was added and the modification for CIOVERLAP module was done by previous work.[75]

3. RESULTS AND DISCUSSION

3.1. The Oxygenation of $\mathbf{I}^{3-}$. As mentioned above, the SET-oxygenation has been considered to be a general process in the oxygen-dependent BL system, and occurs easily for the dianion state of **ImPy**s,[46] so oxygenation of $\mathbf{I}^{3-}$ may be initiated by a SET process from $\mathbf{I}^{3-}$ to $^3O_2$ to produce the superoxide anion $O_2^{\bullet-}$. The change of Gibbs free energy (ΔG_{SET}) of the SET process between $\mathbf{I}^{3-}$ and $^3O_2$ was estimated in gas phase and four solvents with different dielectric coefficients and summarized in Table S1. It can be found that the SET reaction is endergonic in gas phase (ΔG_{SET} = 22.2 kcal mol^{-1}), but mightily exergonic in polar solvents (ΔG_{SET} = −2.8, −21.6, −21.7, and −22.1 kcal mol^{-1} in benzene, CH_3CN, DMSO, and water, respectively). This implies that the SET process is strongly influenced by the surrounding reaction field and probably occurs in a polar solvent thermodynamically. The estimated k_{ET} from $\mathbf{I}^{3-}$ to $^3O_2$ based on Marcus theory were also summarized in Table S1. The estimated value of k_{ET} (6.29×10^8 s^{-1}) gives an evidence that SET can take place easily in DMSO, which is a common polar solvent used in experimental studies of **ImPy**s BL.[26,28] So in the following discussion, the oxygenation of $\mathbf{I}^{3-}$ initiated by SET was investigated in DMSO.

The SET between $^3O_2$ and $\mathbf{I}^{3-}$ in DMSO generates $^3[\mathbf{I}^{\bullet2-}\cdots O_2^{\bullet-}]$.[91−94] The $^3[\mathbf{I}^{\bullet2-}\cdots O_2^{\bullet-}]$ must undergo a spin inversion to produce singlet dioxetanone **III** that is considered to decompose with light emission. Generally, the spin-alignment of $^3[\mathbf{I}^{\bullet2-}\cdots O_2^{\bullet-}]$ occurs via two pathways (Scheme 3). On one

Scheme 3. Two Pathways for the Spin-Alignment of the Exciplex Forming the Singlet-State Dioxetanone Complex $\mathbf{III}^{3-}$

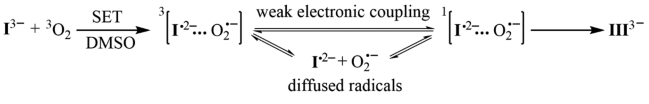

hand, the weak electronic coupling may result in an extremely small energy separation or almost degenerate between $^3[\mathbf{I}^{\bullet2-}\cdots O_2^{\bullet-}]$ and $^1[\mathbf{I}^{\bullet2-}\cdots O_2^{\bullet-}]$, so that the hyperfine interaction between the electron spins and nuclear spins may cause the mixing of $^3[\mathbf{I}^{\bullet2-}\cdots O_2^{\bullet-}]$ and $^1[\mathbf{I}^{\bullet2-}\cdots O_2^{\bullet-}]$, when the electron exchange interaction is smaller than the hyperfine coupling.[95,96] On the other hand, $^3[\mathbf{I}^{\bullet2-}\cdots O_2^{\bullet-}]$ is usually diffused efficiently by bulk solution, then the two free doublet radicals ($\mathbf{I}^{\bullet2-}$ and $O_2^{\bullet-}$) emerge. $^1[\mathbf{I}^{\bullet2-}\cdots O_2^{\bullet-}]$ may be produced via the recombination of $\mathbf{I}^{\bullet2-}$ and $O_2^{\bullet-}$ including spin inversion. As Isobe et al. pointed out, "Provided that there is no spin catalysis by paramagnetic additives such as transition-metal ions, the recombination of freely diffusing radicals is the only pathway for the spin-symmetry-allowed singlet generation from the triplet pair."[46] It is obvious that $^1[\mathbf{I}^{\bullet2-}\cdots O_2^{\bullet-}]$ is crucial for the SET-oxygenation of $\mathbf{I}^{3-}$. The S_0 potential energy curves (PECs) of SET-oxygenations of $\mathbf{I}^{3-}$ at C_2- and C_3-position using $^1[\mathbf{I}^{\bullet2-}\cdots O_2^{\bullet-}]$ as initial state are shown in Figures 1 and 4. The changes of key geometric parameters and the Mulliken charge population on the $O_2^{\bullet-}$ and $\mathbf{I}^{\bullet2-}$ moieties along the two reaction paths were summarized in Figure 2. The electronic states were described with natural orbitals (NOs) and summarized in Tables S2 and S3. The energies of the first triplet excited state (T_1) state ($^3[\mathbf{I}^{\bullet2-}\cdots O_2^{\bullet-}]$ as initial state) based on the points of S_0 PES were displayed in Figures 3 and 5. The PECs of C_2- and C_3-oxygenation of $\mathbf{I}^-$ were displayed in Figures S3 and S4.

3.1.1. The C_2-Oxygenation of I^{3-}. $^1[I^{\bullet2-}\cdots O_2^{\bullet-}]$ as Initial State. As shown in Figure 1, the singlet exciplex, $^1[\mathbf{I}^{\bullet2-}\cdots O_2^{\bullet-}]$ (RC), is formed by electrostatic force and van der Waals interaction on the S_0 PES of C_2-oxygenation. The O_a-O_b bond distance in the RC is 1.236 Å and longer than it in $^3O_2$ (1.205 Å), which implies $O_2^{\bullet-}$ rather than $^3O_2$ attacks the substrate $\mathbf{I}^{3-}$. There is a partial negative charge transferred from $O_2^{\bullet-}$ to $\mathbf{I}^{\bullet2-}$ during the formation of RC, because the Mulliken charge on the $O_2^{\bullet-}$ moiety, $\rho(O_2^{\bullet-})$, changes from −1|e| in $O_2^{\bullet-}$ to −0.32|e| in RC. From RC to the final adduct $\mathbf{III}^{3-}$, four TSs and three Ints were located. Vibrational analysis indicates that TS1(214.6*i*), TS3(151.5*i*), and TS4(155.0*i*) correspond to the stretching of C_2-O_a, C_3-O_b, and C_3-N_4 bond, respectively (see Figure 1). But the imaginary vibrational modes of TS2 (2335.5*i*) could not be obviously attributed to a single imaginary canonical vibrational mode, both C_2-O_a and O_a-O_b stretch synchronously in TS2.

As shown in Figure 2A, the C_2-oxygenation reaction starts with the gradual shortening of C_2-O_a bond along with the torsion of $C_3-C_2-O_a-O_b$ toward to the direction of the closure of four-membered ring. After TS2, the variation curves of C_2-O_a remains almost flat from 4.308 amu$^{1/2}$ bohr until the formation of final product $\mathbf{III}^{3-}$. In the flat region of C_2-O_a bond curve, the C_3-O_b bond and the dihedral $C_3-C_2-O_a-O_b$ keep almost unchanged at the beginning (between 4.308 and 38.010 amu$^{1/2}$ bohr), then changes quickly to form the four-membered ring. Int2 (with 1.399 Å C_2-O_a, −74.2 °$C_3-C_2-O_a-O_b$, and −1.00|e| $\rho(O_2^{\bullet-})$) was located in this platform, which is the 2-peroxide anion. The 2-peroxide was also trapped in previous experimental investigation on the oxygenation of **ImPy**s.[47] In the vicinity of Int3, the variation curves of C_3-O_b and $C_3-C_2-O_a-O_b$ remain flat again, which indicates that the four-membered ring is formed. The C_3-N_4 bond keeps unchanged from the beginning of C_2-oxygention reaction, and starts to break to produce $\mathbf{III}^{3-}$ after Int3 accompanying with the minor adjustments of C_2-O_a and C_3-O_b bonds. So the cleavage of C_3-N_4 bond and the closure of four-membered ring are stepwise. The expectation value of $\mathbf{S}^2$ operator ($\langle S^2\rangle$ in Figure 1) demonstrates that the S_0 state has obvious biradical characteristic from RC to TS2 (1.02 for RC, 1.00 for TS1, 0.99 for Int1, and 0.82 for TS2). The PEC between TS1 and TS2 is very short and almost flat. After TS2, the biradical character of molecule disappears, and the S_0 energy suddenly decreases to form Int2. Among all the energy barriers on the S_0 PEC, the one from RC to Int1 is the highest (9.8 kcal mol^{-1}). So this step is the rate-determining one, whose barrier is 1.4 kcal mol^{-1} lower than that of the C_2-oxygenation of $\mathbf{I}^-$ (shown in Figure S3).

The NOs analysis along the IRC (Table S2) have shown that the NOs are mainly located at the $O_2^{\bullet-}$ moiety in the vicinity of

DOI: 10.1021/jacs.6b09119
J. Am. Chem. Soc. 2017, 139, 1106−1119

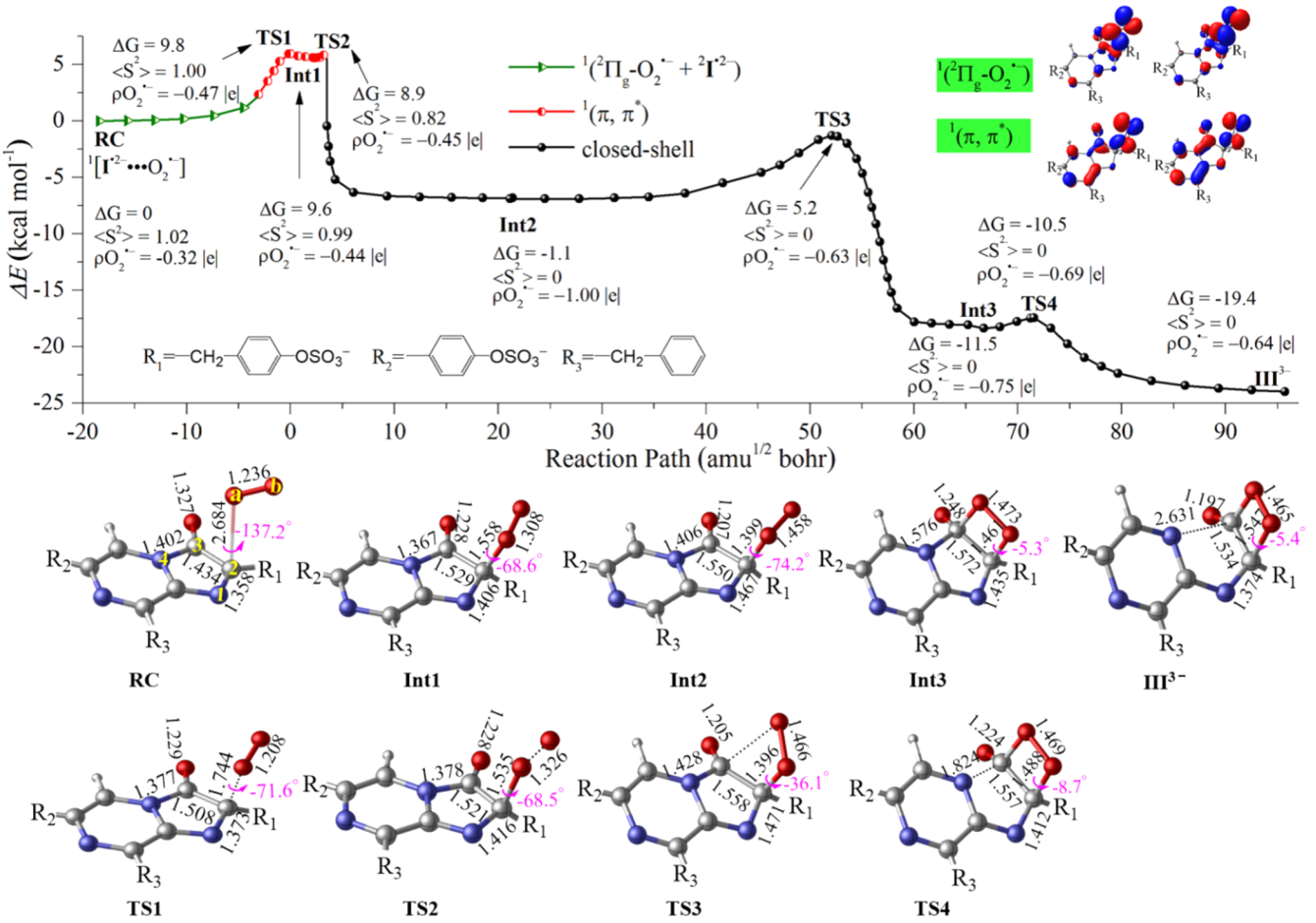

Figure 1. S_0 PEC ($^1[I^{\bullet 2-}\cdots O_2^{\bullet -}]$ as initial state) of C_2-oxygenation of I^{3-} takes place between $I^{\bullet 2-}$ and $O_2^{\bullet -}$ in DMSO computed at the UCAM-B3LYP/6-31G(d,p) level. The key atoms (N_1, C_2, C_3, N_4, O_a, and O_b) are highlighted in yellow, and the dihedral angle ($C_3-C_2-O_a-O_b$) in pink. Here and hereunder, gray, blue, white, and red balls represent carbon, nitrogen, hydrogen, and oxygen atoms, respectively. The units are angstrom (Å) for bond distance, degree (deg) for the dihedral angle, and kcal mol^{-1} for Gibbs energy change (ΔG).

RC. So the S_0 state exhibits $^2\Pi_g$ configuration. With the approaching of $O_2^{\bullet -}$, the degenerate π^* orbital of $O_2^{\bullet -}$ couples with the π orbital distributed in **ImPy** skeleton of $I^{\bullet 2-}$, which brings about the S_0 state of $^1(\pi, \pi^*)$ configuration. Then the S_0 state turns into the closed-shell configuration after TS2. Therefore, S_0 is denoted as $^1(^2\Pi_g\text{-}O_2^{\bullet -} + {}^2I^{\bullet 2-})/^1(\pi, \pi^*)$/closed-shell state. According to the variation of Mulliken population along the IRC (Figure 2C), a gradual CT from $I^{\bullet 2-}$ to $O_2^{\bullet -}$ takes place before TS2, and then followed by a sharply decreasing of the charge of $I^{\bullet 2-}$, $\rho(I^{\bullet 2-})$ ($-2.55|e| \rightarrow -2.08|e|$) and increasing of $\rho(O_2^{\bullet -})$ ($-0.45|e| \rightarrow -0.92|e|$). Afterward, the Mulliken charges showed no obvious variation between 4.308 and 38.010 amu$^{1/2}$ bohr, where the $\rho(O_2^{\bullet -})$ remains nearly $-1|e|$. It fully proves the existence of 2-peroxide anion in conjugation with the key geometric parameters (Figure 2A). Then a gradual BCT process from $O_2^{\bullet -}$ to $I^{\bullet 2-}$ takes place from TS3 to the final product III^{3-}. The $\rho(O_2^{\bullet -})$ and $\rho(I^{\bullet 2-})$ located at the product III^{3-} is $-0.64|e|$ and $-2.36|e|$ (Figure 1). The C_2-oxygenation pathway is consistent with experimental observation of the two complex signals (2-peroxide and dioxetanone intermediates) by ^{13}C NMR spectroscopy.[47] It is noteworthy that the distance of C_2-O_a bond in Int1 is 1.558 Å and in III^{3-} is 1.547 Å (Figure 1), which indicates that the C_2-O_a bond is already formed in Int1. But Int1 has biradical character ($\langle S^2\rangle$ = 0.99), and then produces to the 2-peroxide anion (Int2) via TS2, which implies that the 2-peroxide anion is formed via a nucleophilic addition followed by TS2 with biradical annihilation rather than the generally proposed radical coupling in coelenterate,[53] *Cypridina*.[49]

$^3[I^{\bullet 2-}\cdots O_2^{\bullet -}]$ as Initial State. As shown in Figure 3, at beginning, the T_1 state takes on $^2\Pi_g$ configuration, then changes to $^3(n, \pi^*)$. Here, n is the p orbitals of O_a and O_b atoms, and π^* orbital mainly represents the π-antibonding orbital of **ImPy** ring in $I^{\bullet 2-}$. Finally, the T_1 state turns into $^3(\pi, \pi^*)$ configuration with the formation of four-membered ring. The π and π^* distribute in **ImPy** ring. So T_1 is represented as $^3(^2\Pi_g\text{-}O_2^{\bullet -} + {}^2I^{\bullet 2-})/^3(n, \pi^*)/^3(\pi, \pi^*)$. The energies in the S_0 and T_1 states are almost degenerate in the short and flat biradical region (between TS1 and TS2), and the two PECs begin to separate after TS2, which implies a S/T surface intersection nearby TS2. Unfortunately, the currently employed method does not have the capability to optimize the geometry of S/T crossing point, and the multiconfiguration method is not available to handle such a large system. According to Figure 3, $^1III^{3-}$ may be produced by $^3[I^{\bullet 2-}\cdots O_2^{\bullet -}]$ via two pathways. In the first way, $^3III^{3-}$ is produced from $^3[I^{\bullet 2-}\cdots O_2^{\bullet -}]$ by overcoming a barrier of 59.2 kcal mol^{-1}. Then, $^1III^{3-}$ is formed after $^3III^{3-}$ undergoes a ISC process. In the second way shown by cyan arrow in Figure 3, $^1III^{3-}$ is formed directly by $^3[I^{\bullet 2-}\cdots O_2^{\bullet -}]$ via the ISC at the S/T crossing point, which needs to overcome a barrier of 12.2 kcal mol^{-1}. The barrier of the second way is much lower than that of the first way. Moreover,

DOI: 10.1021/jacs.6b09119
J. Am. Chem. Soc. 2017, 139, 1106−1119

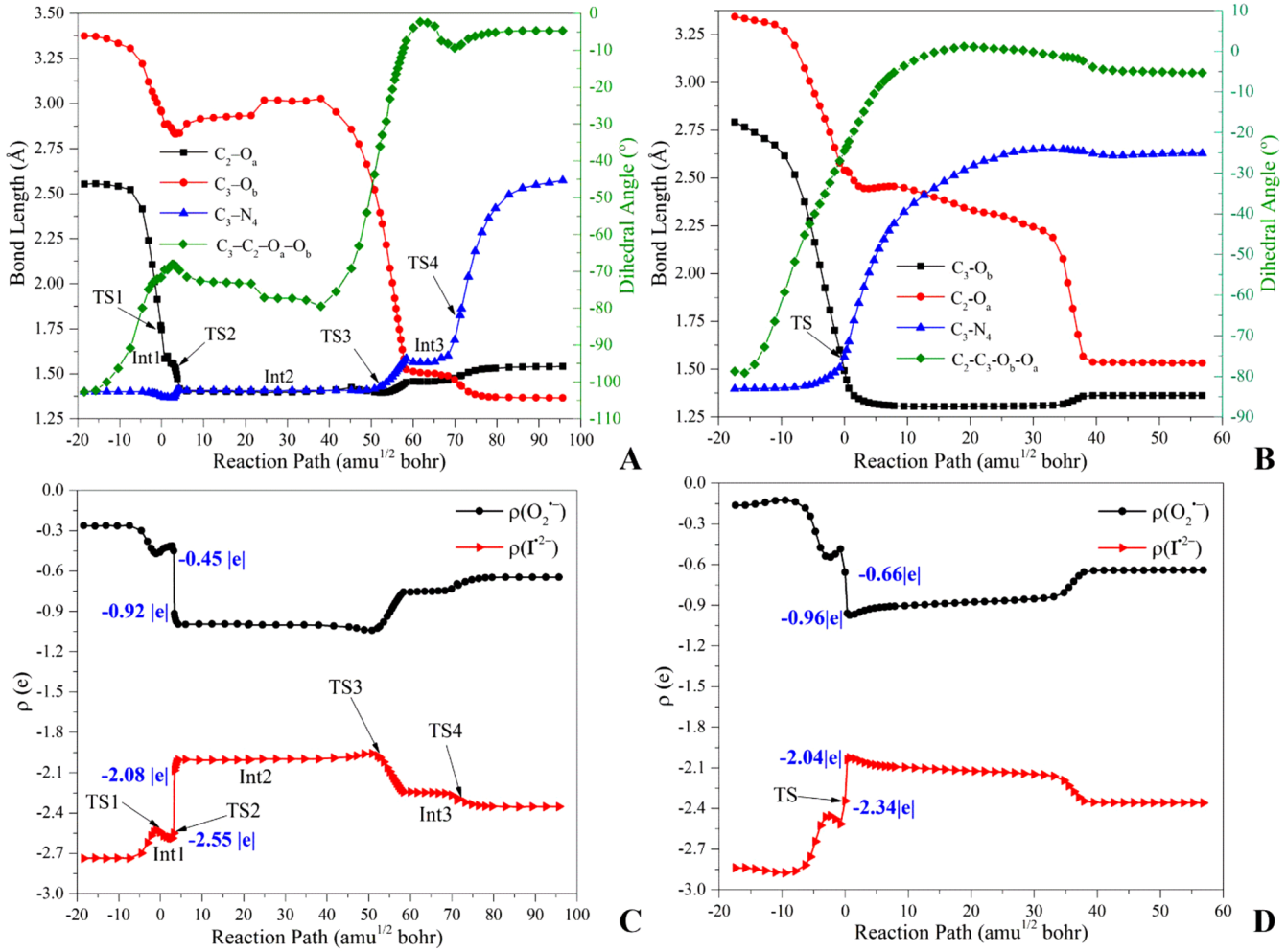

Figure 2. Key geometric parameters and the Mulliken charges on the $O_2^{\bullet-}$ and $\mathbf{I}^{\bullet 2-}$ moieties in the C_2-oxygenation (A, C) and C_3-oxygenation (B, D) pathways along the IRC calculated in DMSO at the UCAM-B3LYP/6-31G(d,p) level.

on the basis of El-Sayed's rule, the rate of ISC is relatively large when the transition involves a change of molecular orbital type.[97] A change of the molecular orbital type indeed exists in the second way ($^3(n, \pi^*)$ and $^1(\pi, \pi^*)$ in the degenerate region around TS2) as shown in Figure 3. So $^1\mathbf{III}^{3-}$ prefers to be formed from $^3[\mathbf{I}^{\bullet 2-}\cdots O_2^{\bullet-}]$ via the second way.

3.1.2. The C_3-Oxygenation of I^{3-}. $^1[I^{\bullet 2-}\cdots O_2^{\bullet-}]$ as Initial State. As shown in Figure 4, the singlet exciplex, $^1[\mathbf{I}^{\bullet 2-}\cdots O_2^{\bullet-}]$ (RC), is located in C_3-oxygenation pathway with the C_3-O_b bond of 2.792 Å. The distance of O_a-O_b (1.223 Å) and the negative charges −0.15|e| indicate that $\mathbf{I}^{3-}$ is oxidized by $O_2^{\bullet-}$ instead of $^3O_2$, and that partial negative charges are transferred from $O_2^{\bullet-}$ to $\mathbf{I}^{\bullet 2-}$ with the approaching of $O_2^{\bullet-}$, which is similar to the C_2-oxygenation pathway. However, from singlet RC, only one TS (1100.5*i*) is located, which corresponds to the simultaneous stretching of C_3-O_b and C_3-N_4 bond. There is no peroxide intermediate formed, which is different from the C_2-oxygenation pathway.

On the basis of the variations of dominant geometric parameters in Figure 2B, the C_3-oxygenation reaction starts with the formation of C_3-O_b along with the torsion of $C_2-C_3-O_b-O_a$ toward to the direction of the closure of the four-membered ring. After TS, a platform appears on the variation curve of C_3-O_b from 1.519 $amu^{1/2}$ bohr to the formation of final product, which is similar to the situation of the C_2-oxygenation. Different to the C_2-oxygenation pathway, in this flat region, the C_2-O_a bond is getting shorter and C_3-N_4 getting longer to produce the final product $\mathbf{III}^{3-}$ directly. So the 3-peroxide anion does not exist in this process. This also indicates that the cleavage of C_3-N_4 bond and the closure of four-membered ring are concerted. The $\langle S^2\rangle$ (Figure 4) demonstrates that S_0 state has obvious biradical characteristics from RC (0.94) to TS (0.55), but the biradical character of molecule disappears after TS. The activation barrier of C_3-oxygenation is 18.4 kcal mol^{-1}, which is 0.8 kcal mol^{-1} lower than that of the C_3-oxygenation of $\mathbf{I}^-$ (see Figure S4), but 8.6 kcal mol^{-1} higher than that of the C_2-oxygenation of $\mathbf{I}^{3-}$. So from the viewpoint of thermodynamics, the C_2-oxygenation of $\mathbf{I}^{3-}$ is energetically feasible using $^1[\mathbf{I}^{\bullet 2-}\cdots O_2^{\bullet-}]$ as initial state.

Similar to the case of C_2-oxygenation, the S_0 state behaves a $^2\Pi_g$ configuration, then gradually presents (π, π^*) configuration along with the mixing between π^* orbital of $O_2^{\bullet-}$ and π orbital of the **ImPy** ring in $\mathbf{I}^{\bullet 2-}$. After TS, the S_0 state turns into the closed-shell configuration in which all of the bonding and nonbonding orbitals are doubly occupied. So the S_0 state is denoted as $^1(^2\Pi_g\text{-}O_2^{\bullet-} + {}^2\mathbf{I}^{\bullet 2-})/^1(\pi, \pi^*)$/closed-shell state. Correspondingly, the charge gradually transfers from $\mathbf{I}^{\bullet 2-}$ to $O_2^{\bullet-}$ moieties in the vicinity of RC accompanied by the formation of the first C−O bond (i.e., C_3-O_b bond) as shown in Figure 2D. After TS2, $\rho(O_2^{\bullet-})$ sharply increases from −0.66|

DOI: 10.1021/jacs.6b09119
J. Am. Chem. Soc. 2017, 139, 1106−1119

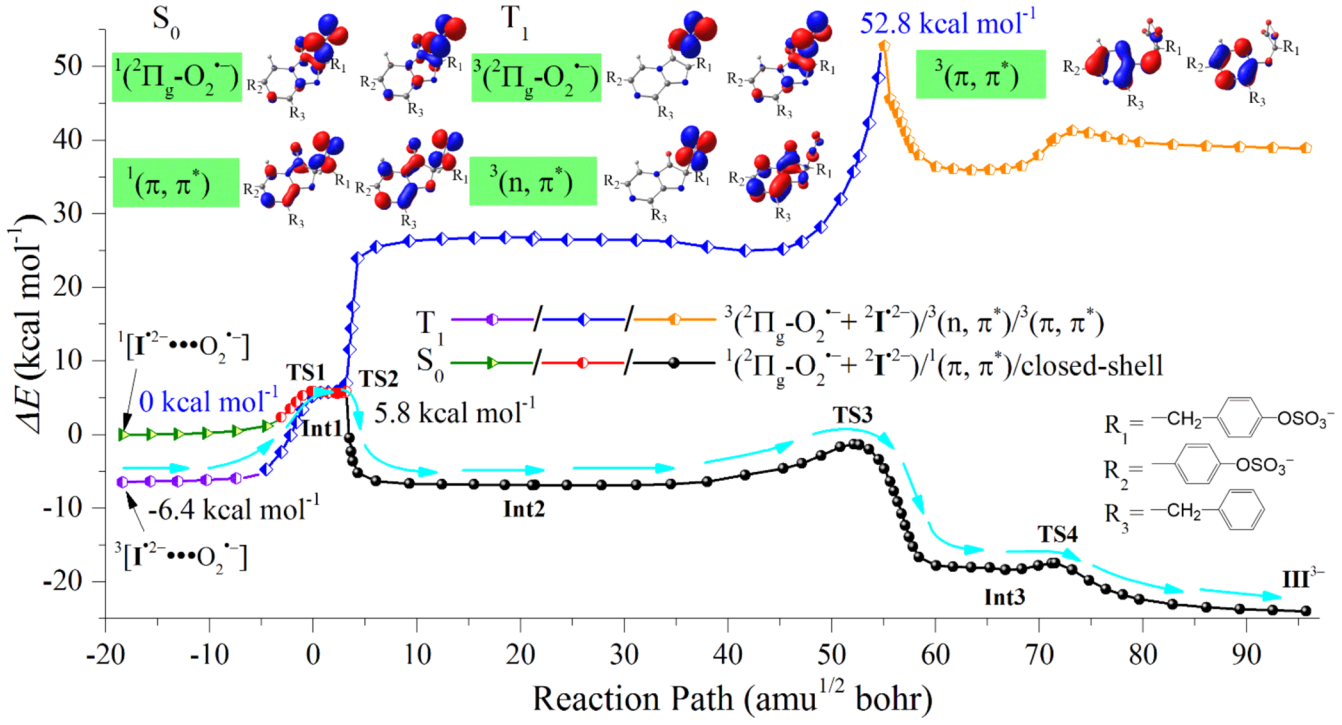

Figure 3. S_0 and T_1 PECs of the C_2-position oxygenation of $\mathbf{I}^{3-}$ in DMSO calculated at the UCAM-B3LYP/6-31G(d,p) level.

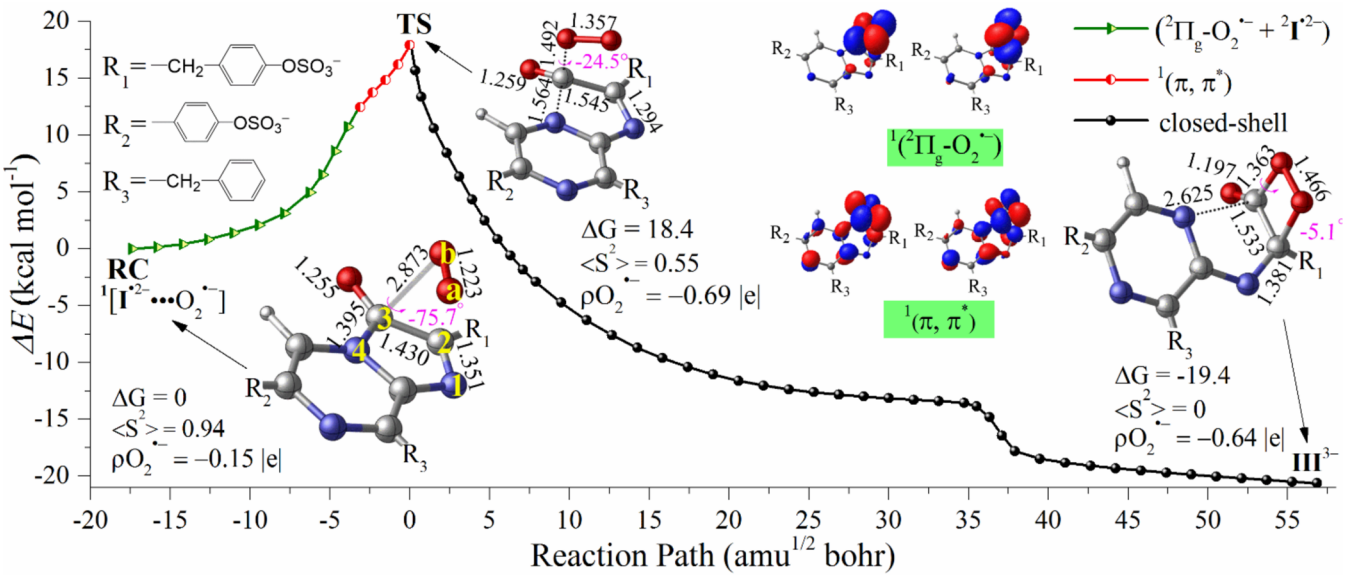

Figure 4. S_0 PEC ($^3[\mathbf{I}^{\bullet 2-}\cdots O_2^{\bullet -}]$ as initial state) of C_3-oxygenation of $\mathbf{I}^{3-}$ occurs between $\mathbf{I}^{\bullet 2-}$ and $O_2^{\bullet -}$computed in DMSO at the UCAM-B3LYP/6-31G(d,p) level. The key atoms (N_1, C_2, C_3, N_4, O_a and O_b) are highlighted in yellow, and the dihedral angle ($C_2-C_3-O_b-O_a$) in pink.

e| to −0.96|*e*|, and correspondingly, $\rho(\mathbf{I}^{\bullet 2-})$ decreases from −2.34|*e*| to −2.04|*e*|. Then there is a gradual BCT from $O_2^{\bullet -}$ to $\mathbf{I}^{\bullet 2-}$ coupled with the formation of the four-membered ring.

$^3[\mathbf{I}^{\bullet 2-}\cdots O_2^{\bullet -}]$ as Initial State. According to the NOs analysis, the T_1 state (Figure 5) changes from the $^2\Pi_g$ configuration (near the RC) to the (n, π^*) configuration, and takes on a little (π, π^*) configuration neighboring the rupture of C_3-N_4 bonds from 35.508 to 36.304 amu$^{1/2}$ bohr. So the T_1 is denoted as $^3(^2\Pi_g\text{-}O_2^{\bullet -}+ {}^2\mathbf{I}^{\bullet 2-})/^3$(n, π^*)/^{3}(π, π^*) state. Similar to the C_2-oxygenation, the T_1 state is almost degenerate with the S_0 state near TS. After TS, the energies of the T_1 state are apparently higher than those of the S_0 state. This also implies a S/T surface intersection around TS. $^3[\mathbf{I}^{\bullet 2-}\cdots O_2^{\bullet -}]$ can generate $^1\mathbf{III}^{3-}$ via two pathways. (1) $^3[\mathbf{I}^{\bullet 2-}\cdots O_2^{\bullet -}]$ needs to pass over a barrier of 71.8 kcal mol^{-1} to form $^3\mathbf{III}^{3-}$, then $^3\mathbf{III}^{3-}$ undergoes a ISC to produce $^1\mathbf{III}^{3-}$ (Figure 5). (2) $^3[\mathbf{I}^{\bullet 2-}\cdots O_2^{\bullet -}]$ overcomes a barrier of 26.3 kcal mol^{-1} then goes through a ISC near TS to form $^1\mathbf{III}^{3-}$ (the cyan arrow in Figure 5). The latter pathway has much lower barrier. And the transition between ^{1}(π, π^*) and ^{3}(n, π^*) is much likely to occur in the vicinity of TS based on the El-sayed's rule. Hence, $^1\mathbf{III}^{3-}$ is probably produced via ISC through this S/T crossing point near TS from $^3[\mathbf{I}^{\bullet 2-}\cdots O_2^{\bullet -}]$.

DOI: 10.1021/jacs.6b09119
J. Am. Chem. Soc. 2017, 139, 1106−1119

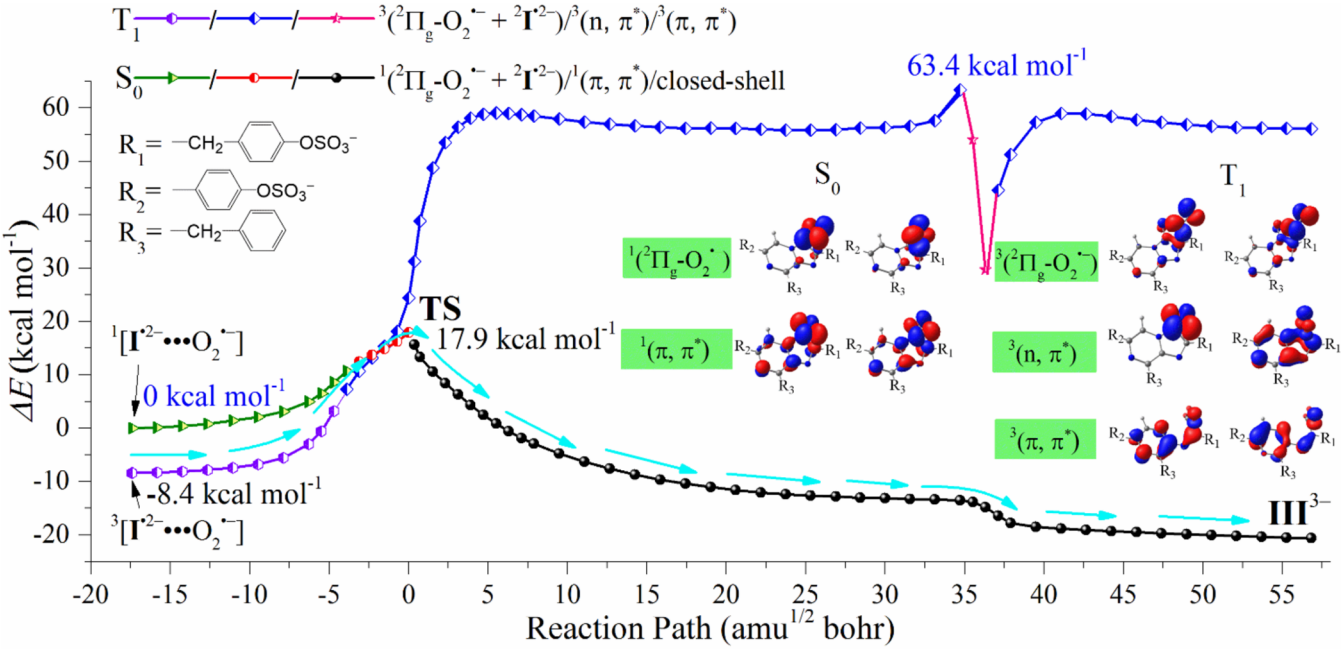

Figure 5. S_0 and T_1 PECs of the C_3-position oxygenation of $\mathbf{I}^{3-}$ in DMSO calculated at the UCAM-B3LYP/6-31G(d,p) level.

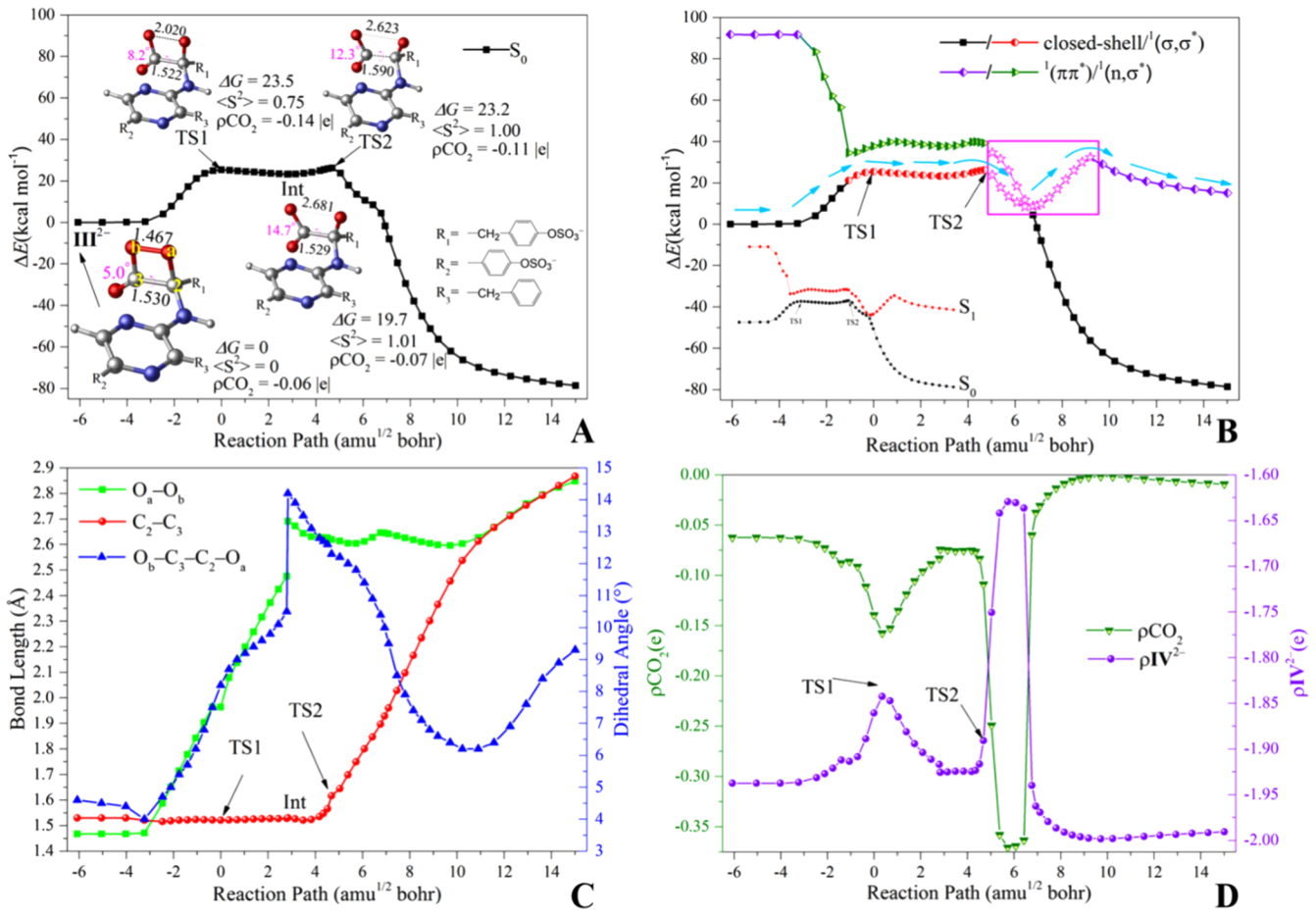

Figure 6. (A) The S_0 PECs for $\mathbf{III}^{2-}$ decomposition; (B) The approximate diabatic PECs of the $^1(\sigma, \sigma^*)$, $^1(\pi, \pi^*)$, and $^1(n, \sigma^*)$ states with the adiabatic PECs of the S_0 and S_1 states (inset); (C) The variation of key geometric parameters; (D) The populations of Mulliken charges on CO_2 and $\mathbf{IV}^{2-}$ along the IRC computed in gas phase at the UCAM-B3LYP/6-31G(d,p) level. The key atoms (C_2, C_3, O_a, and O_b) are highlighted in yellow, and the dihedral angle (O_b–C_3–C_2–O_a) in pink.

DOI: 10.1021/jacs.6b09119
J. Am. Chem. Soc. 2017, 139, 1106–1119

3.1.3. C_2-Oxygenation vs C_3-Oxygenation. As discussed above, in formation process of ^{1}**III**$^{3-}$ from $^1[\mathbf{I}^{\bullet 2-}\cdots O_2^{\bullet -}]$, the 2-peroxide anion is formed, so the C_2-oxygenation of $\mathbf{I}^{3-}$ is stepwise. The C_3-oxygenation is concerted because there is not any peroxide anion formed. This can also be found by comparing the changes of the C_3-N_4 bond and the closure of the four-membered ring. The C_2-oxygenation is energetically feasible and agrees with experimental conclusion on 2-peroxide and dioxetanone.[47] The assumption of radical-coupling reaction between $O_2^{\bullet -}$ and $\mathbf{I}^{\bullet 2-}$ (or luminescent substrate radical)[49,53] is not supported by current results. Int2 is directly transformed from Int1 via nucleophilic addition followed by TS2 of biradical annihilation rather than by the coupling of $O_2^{\bullet -}$ and $\mathbf{I}^{\bullet 2-}$ radicals in C_2-oxygenation. However, the spin−orbital coupling cannot be achieved by the current theoretical method, so the formation rate of ^{1}**III**$^{3-}$ from $^3[\mathbf{I}^{\bullet 2-}\cdots O_2^{\bullet -}]$ was not computed. Nevertheless, $^3[\mathbf{I}^{\bullet 2}\cdots O_2^{\bullet -}]$ needs about 26.3 kcal mol^{-1} to approach the C_3−ISC, which is much higher than that to the C_2−ISC (12.2 kcal mol^{-1}). Using $^3[\mathbf{I}^{\bullet 2-}\cdots O_2^{\bullet -}]$ as the initial RC, the C_2-oxygenation state is energetically more feasible than C_3-oxygenation. But we do not have strong evidence to judge whether $^1[\mathbf{I}^{\bullet 2-}\cdots O_2^{\bullet -}]$ or $^3[\mathbf{I}^{\bullet 2-}\cdots O_2^{\bullet -}]$ is more favorable in C_2-oxygenation based on the current calculations.

3.2. The Chemiluminescent Decomposition of *W. scintillans* Dioxetanone III. The thermolysis and chemiexcitation mechanisms of both $\mathbf{III}^{2-}$ and $\mathbf{III}^{3-}$ were considered in gas phase and DMSO. The calculated PECs of S_0 and S_1 states, key geometric parameters, and the populations of Mulliken charges were depicted in Figures 6 and 7. Time evolution of the average distribution of the O_a-O_b and C_2-C_3 bond distances, the Mulliken charges of CO_2 and $\mathbf{IV}^{2-}/\mathbf{IV}^{3-}$ moieties, and the fractional occupations of the S_0 and S_1 states during the TSH simulation were shown in Figures 8 and 9, respectively. The comparisons of the S_0 PECs in gas phase and DMSO for $\mathbf{III}^{2-}$ and $\mathbf{III}^{3-}$ decompositions were shown in Figure S6. The main NOs changes during $\mathbf{III}^{2-}$ and $\mathbf{III}^{3-}$ decompositions were summarized in Tables S4 and S5. For comparison, the decompositions of **III** and $\mathbf{III}^-$ with $(-OSO_3H)_2$ were further investigated and related data were summarized in Figures S5, S7, S10, and S11.

3.2.1. Thermolysis and Chemiexcitation of $\mathbf{III}^{2-}$. Two TSs and one Int were located on the S_0 PES during the thermolysis of $\mathbf{III}^{2-}$ in gas phase (Figure 6A). The imaginary vibrational modes of TS1 (438.8*i*) and TS2 (1067.3*i*) correspond to the stretching of O_a-O_b and C_2-C_3 bond, respectively. As shown in Figure 6C, the decomposition of $\mathbf{III}^{2-}$ starts with the elongation of O_a-O_b bond. But a platform appears on the variation curve of O_a-O_b bond between 2.841 and 10.903 amu$^{1/2}$ bohr. In this region, the O_a-O_b bond distance is about 2.7 Å, which indicates that the O_a-O_b bond is completely ruptured. The C_2-C_3 bond keeps unchanged from the beginning of $\mathbf{III}^{2-}$decomposition (Figure 6C), then begins to elongate to form final product $\mathbf{IV}^{2-}$ after 4.176 amu$^{1/2}$ bohr. An Int (O_a-O_b of 2.681 Å and C_2-C_3 of 1.529 Å) was located in this flat stage. These results indicate that the $\mathbf{III}^{2-}$ decomposition is a typical stepwise process, which is similar to the neutral decomposition of simple dioxetanones.[30,31,62,65−67] The dihedral angles of $O_b-C_3-C_2-O_a$ (5.0° in $\mathbf{III}^{2-}$, 8.2° in TS1, 14.7° in Int, 12.4° in TS2) indicate that the four-membered ring keeps nearly planar during the whole process. The $\langle S^2\rangle$ values (0.75 for TS1, 1.00 for TS2, 1.01 for Int in Figure 6A) demonstrates that TS1, TS2, and Int all have obvious biradical characters. The S_0 PEC between TS1 and TS2 is nearly flat with biradical characteristic. The energy barriers from $\mathbf{III}^{2-}$ to Int and the final product are 23.5 and 23.2 kcal mol^{-1}, respectively. So the first step is the rate-determining step, which is in line with the experimental results of other dioxetanes and dioxetanones (about 20.0 kcal mol^{-1} see SI in ref 30). As shown in Figure 6D, there is no obvious CT from $\mathbf{IV}^{2-}$ to CO_2 (<0.1|*e*|) moiety on the S_0-state PEC. But a sudden CT/BCT about −0.30|*e*| appears between 4.691 and 6.765 amu$^{1/2}$ bohr, which is different from non-CT decompositions of the simple dioxetanones.[30,31,65−67]

According to the adiabatic PECs (the inset in Figure 6B), the S_0 and S_1 curves approach close to each other as the elongation of O_a-O_b bond, and then becomes nearly parallel at the biradical platform region between −1.055 and 4.692 amu$^{1/2}$ bohr. The NOs analysis (Table S4) along the IRC indicates that S_0 surface gradually changes from closed-shell to $^1(\sigma, \sigma^*)$ configuration, while S_1 state changes from $^1(\pi, \pi^*)$ to $^1(n, \sigma^*)$ configuration before TS2. Here σ and σ^* correspond to the bonding and antibonding molecular orbitals of O_a-O_b bond, and n refers to the out-of-plane atomic p orbital of O_a and in-plane atomic p orbital of O_b. The π and π^* orbital are mainly contributed by the pyrazine ring. These variations of electronic structure are similar to those neutral decompositions of previously studied dioxetanones,[30,31,65−67] where nearly degenerated $^1(\sigma,\sigma^*)$ and $^1(n,\sigma^*)$ PECs were located during the flat biradical region.[30,31,61,64] However, the interval of the S_0 and S_1 PECs is large rather than small at the flat biradical region (Figure 6B). The energetic error is caused by the UTDDFT calculation, which is not able to describe the open-shell biradical as a single configuration method. The SF-DFT calculations can dramatically reduce the interval at the flat region although it is still not an ideal way to handle the biradical systems (see Figure S2A in section 3 of SI). The problem frequently occurs to the thermolysis of dioxetanones, for examples, the dioxetanones of firefly[30] and *Cypridina*.[31] For the firefly dioxetanone, the UTDDFT calculation predicted a large S_0/S_1 energy gap (more than 20 kcal mol^{-1}) at the flat biradical region, although its computed electronic structures and shapes of the S_0 and S_1 PECs (Figure S11A in ref 30) agree with the ones (Figure 2A in ref 30) calculated by the multireference method, respectively. Nevertheless, the large S_0/S_1 energy gap dramatically decreases after the energy correction by the multireference methods. The UTDDFT is qualitatively reliable for analyzing the thermolysis of dioxetanones. To describe the $\mathbf{III}^{2-}$ decomposition with quantitative accuracy, a multi-reference method has to be adopted as we have done on the firefly dioxtanone.[30] However, it is nearly impossible for such a large system as $\mathbf{III}^{2-}$. On the basis of our previous studies on the decompositions of several dioxetanones,[30,31,61,64] the nearly degenerated S_0/S_1 PECs at the flat region are expected. In the nearly barrierless region, the reaction is mainly driven by the entropic effect and follows entropic trapping mechanism, which compels the reaction molecule to spend a long time passing through the PEC. The nearly degenerated S_0/S_1 PECs could provide the possibility for the nonadiabatic coupling as reported in previous studies.[30] Moreover, with the C_2-C_3 bond cleavage after TS2, the π orbital of pyrazine ring coupled with the p orbital of N_1 and the σ^* orbital of O_a-O_b bond, which brings some $^1(\pi, \sigma^*)$ character into the original $^1(\sigma, \sigma^*)$ configuration of the S_0 state and the $^1(\sigma, \sigma^*)$ configuration of the S_1 state. These states mixing between 5.038 and 9.192 amu$^{1/2}$ bohr (pink box in Figure 6B) leads to a CT character on the S_0 surface as observed in Figure 6D and a smaller S_0/S_1 energy gap

DOI: 10.1021/jacs.6b09119
J. Am. Chem. Soc. 2017, 139, 1106−1119

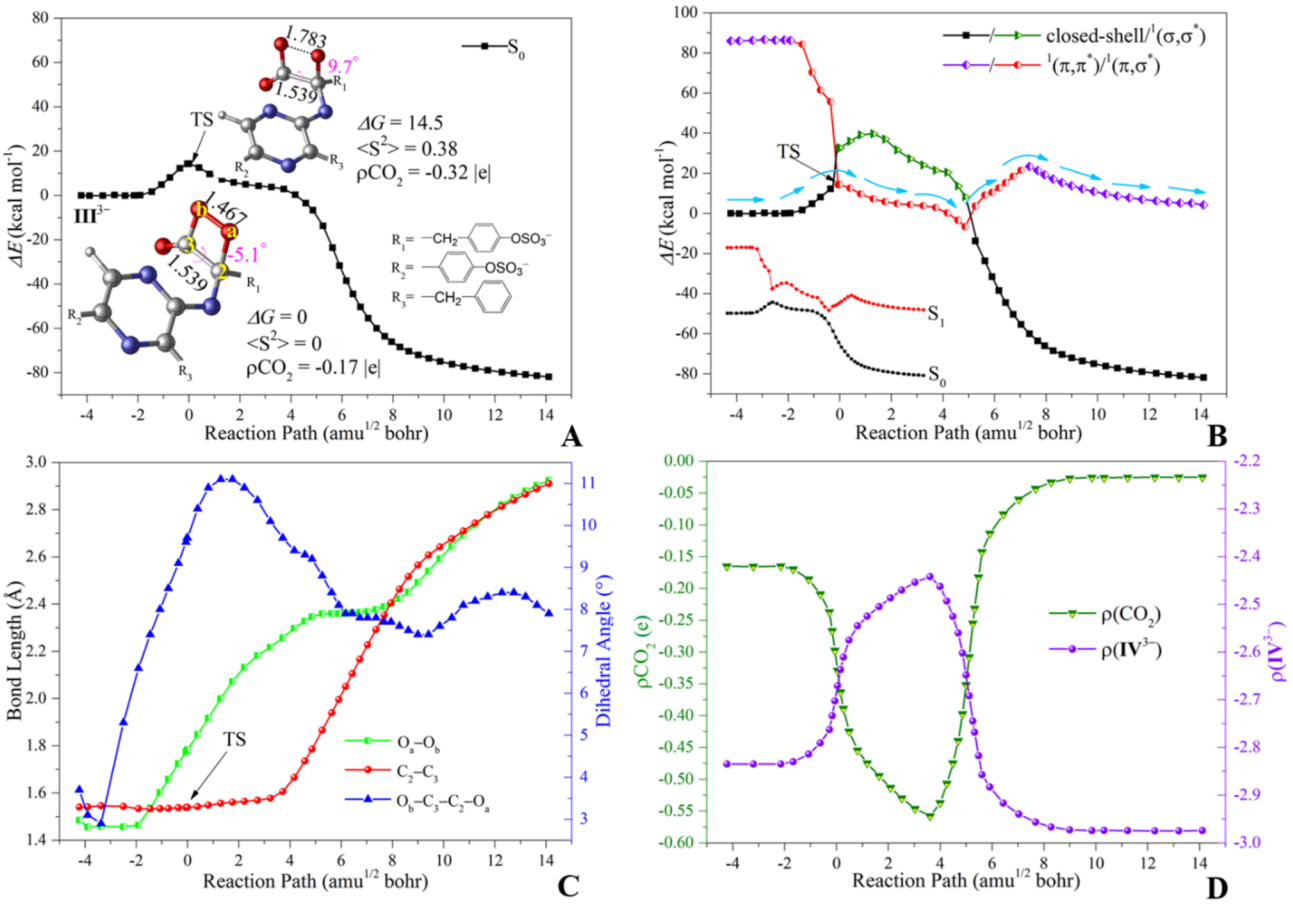

Figure 7. (A) The S_0 PEC for $\mathbf{III}^{3-}$ decomposition; (B) The approximate diabatic PECs of the $^1(\sigma, \sigma^*)$, $^1(\pi, \pi^*)$, and $^1(\pi, \sigma^*)$ states with the adiabatic PECs of the S_0 and S_1 states (inset); (C) The changes of key geometric parameters (O_a–O_b and C_2–C_3 in Å, O_b–C_3–C_2–O_a in degrees labeled in pink); (D) The populations of Mulliken charges on the CO_2 and $\mathbf{IV}^{3-}$ moieties along the IRC computed in gas phase at the UCAM-B3LYP/6-31G(d,p) level. The key atoms (C_2, C_3, O_a, and O_b) are highlighted in yellow, and the dihedral angle (O_b–C_3–C_2–O_a) in pink.

(ΔE = 3.2 kcal mol^{-1}) at 6.423 amu$^{1/2}$ bohr (Figure 6B), which is different to the neutral decompositions of simple dioxetanones.[30,31,65−67] This might be attributed to the two negative charges populated on the two − OSO_3^-, which increases the redox potential of $\mathbf{III}^{2-}$. For comparison, we also investigated the chemiluminescent decomposition of **III**. A similar stepwise biradical process (Figure S5A) without no obvious CT was observed. As shown in Figure S5B, the S_0 and S_1 state of **III** are dominated by the non-CT closed-shell/$^1(\sigma,\sigma^*)$ and $^1(n,\pi^*)/^1(n,\sigma^*)$ configuration without obvious $^1(\pi, \sigma^*)$ configuration, which is very similar to the neutral decomposition of *Cypridina*[31] and firefly dioxetanone.[30]

To sum up, with the influence of the two $-OSO_3^-$, the decomposition and chemiexcitation process of $\mathbf{III}^{2-}$ is a little different to the neutral decompositions of simple dioxetanones. However, the thermolysis of $\mathbf{III}^{2-}$ can also take place via a stepwise-biradical process and its chemiexcitation process could be understood with the entropic trapping mechanism, which is similar to multireference-calculations of the neutral dioxetanones.[30,31,65−67] As shown in Figure S6A, the S_0 PEC is almost unaffected by DMSO, as there is no obvious CT in the $\mathbf{III}^{2-}$ decomposition.

3.2.2. Thermolysis and Chemiexcitation of $\mathbf{III}^{3-}$. As shown in Figure 7A, only one TS with large imaginary frequency (1172.6*i*) was located on the S_0 PES at the UCAM-B3LYP/6-31G(d,p) level, which corresponds to the stretching of O_a–O_b bond. The decomposition of $\mathbf{III}^{3-}$ starts with the elongation of O_a–O_b peroxide bond (Figure 7C) like the $\mathbf{III}^{2-}$ thermolysis. Then a short plateau exists between 5.259 and 7.678 amu$^{1/2}$ bohr in the variation curve of O_a–O_b bond. Different to the $\mathbf{III}^{2-}$ decomposition, in this region, the O_a–O_b bond distance is about 2.3 Å, which indicates that the O_a–O_b bond does not break completely. The C_2–C_3 bond begins to break in the period of stagnation of the O_a–O_b variation curve instead of keeping unchanged in the $\mathbf{III}^{2-}$ thermolysis. So the cleavages of O_a–O_b and C_2–C_3 bonds proceed in an asynchronous-concerted fashion. In addition, the dihedral angle of O_b–C_3–C_2–O_a changes from 3.0° to 11.5°, finally back to 7.8°, which indicates that the four-membered ring remains nearly planar during the $\mathbf{III}^{3-}$ decomposition. The $\langle S^2 \rangle$ (0.38) and $\rho(CO_2)$ ($\mathbf{III}^{3-}$ → TS is −0.32|*e*| → −0.17|*e*|) of TS indicate that it has some biradical and CT characteristics. The activation energy over the TS is 14.5 kcal mol^{-1}, which is 9.0 kcal mol^{-1} lower than that in $\mathbf{III}^{2-}$ decomposition, 7.2 kcal mol^{-1} lower than that in **III** decomposition (Figure S5A), and 1.3 kcal mol^{-1} lower than that in $\mathbf{III}^{-}$decomposition (Figure S7A). Hence the decomposition of $\mathbf{III}^{3-}$ is energetically more feasible for *W. scintillans* BL in terms of the thermodynamics. Moreover, the variations of Mulliken charges (Figure 7D) suggest a gradual CT of $\mathbf{IV}^{3-}$ → CO_2 with $\Delta\rho$ = −0.39|*e*| from −4.227 to 3.608 amu$^{1/2}$ bohr and a gradual BCT of CO_2 → $\mathbf{IV}^{3-}$ with $\Delta\rho$ = −0.53|*e*| from 3.608 to 14.113 amu$^{1/2}$ bohr. In one word, the thermolysis of $\mathbf{III}^{3-}$ is a planar asynchronous-concerted process with CT character, which is similar to the anionic

DOI: 10.1021/jacs.6b09119
J. Am. Chem. Soc. 2017, 139, 1106−1119

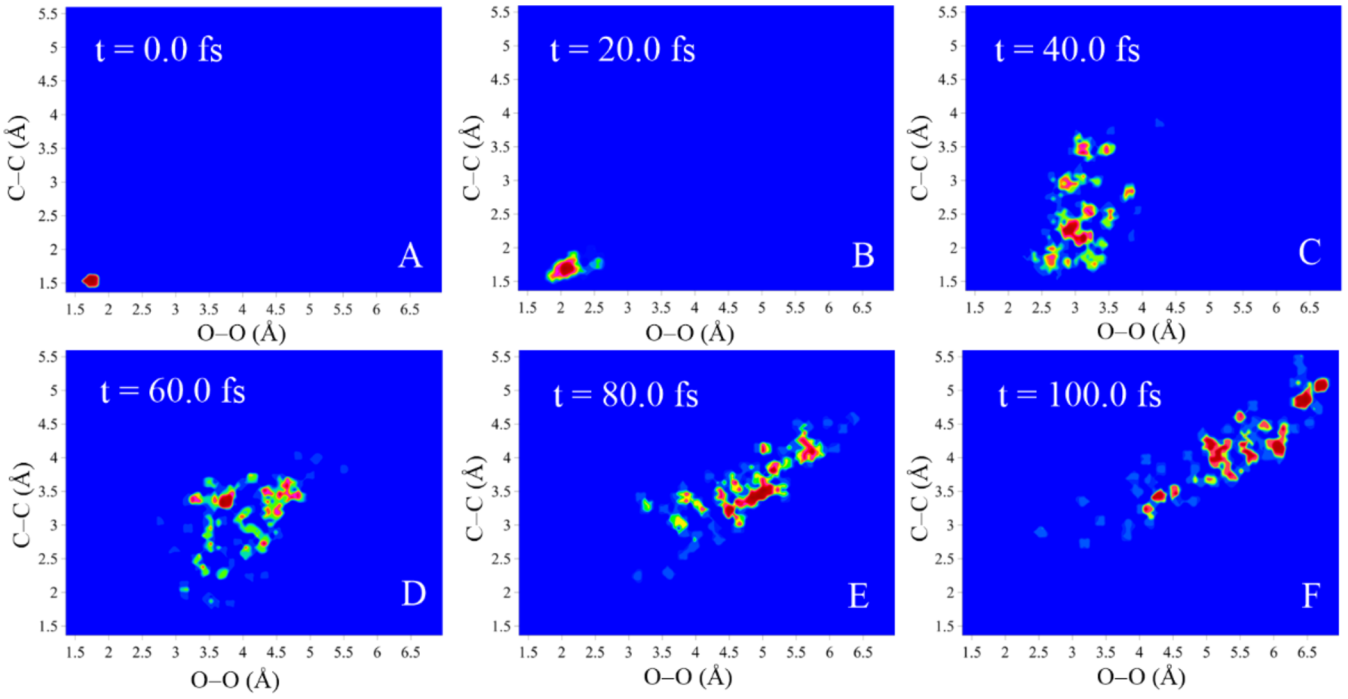

Figure 8. Time evolution of the average distribution of the O_a-O_b and C_2-C_3 bond distances at 0, 20, 40, 60, 80, and 100 fs during the dynamics simulation of $\mathbf{III}^{3-}$ (average over 100 trajectories) obtained by the TSH dynamics in gas phase at the SF-BHHLYP/6-31G(d,p) level.

decomposition of other dioxetanones like FDO^-[30] and CDO^-.[31]

According to the NOs analysis (Table S5), the S_0 state changes from the closed-shell to $^1(\pi, \sigma^*)$ configuration along with the gradual elongation of O_a-O_b bond, which is different from $\mathbf{III}^{2-}$ decomposition. Here π denotes the pπ-conjugated orbital of N_1 and the pyrazine ring, and π^* represents the π-antibonding orbital of pyrazine ring. But in the initial stage, the main configuration of the S_1 state is $^1(\pi, \pi^*)/^1(\pi, \sigma^*)$, but changes to $^1(\sigma, \sigma^*)$ with the rupture of O_a-O_b bond. After the complete rupture of C_2-C_3 bond, the S_1 state changes to $^1(\pi, \pi^*)$ configuration and the S_0 state returns to closed-shell configuration again. Here π and π^* stand for the bonding and antibonding molecular orbitals located in the benzopyrazine ring. So the S_0 and S_1 states can be approximately described by the closed-shell/$^1(\sigma, \sigma^*)$ and $^1(\pi, \pi^*)/^1(\pi, \sigma^*)/^1(\sigma, \sigma^*)$ configurations, respectively. (Figure 7B) The approximate diabatic PECs clearly shows a "double crossings" between the closed shell/$^1(\sigma, \sigma^*)$ and $^1(\pi, \pi^*)/^1(\pi, \sigma^*)/^1(\sigma, \sigma^*)$ surface, which provides the channels for nonadiabatic transition. The smallest energy gaps of S_0 and S_1 states in the vicinities of the double crossings are 17.7 and 15.0 kcal mol^{-1} at IRC = −0.060 and 4.860 $amu^{1/2}$ bohr, respectively, which could be larger than the physical truth due to the spin contamination mentioned in $\mathbf{III}^{2-}$ decomposition. The multiconfiguration methods can decrease the energy gap, but cannot be adopted to treat with such a big system ($\mathbf{III}^{3-}$). A smaller energy gap about 0−3 kcal mol^{-1} was found via the SF-DFT calculations (see Figure S2B in section 3 of SI). In addition, the gradual CT/BCT takes place simultaneously with the O_a-O_b and C_2-C_3 bond cleavages, respectively. Therefore, the decomposition process of $\mathbf{III}^{3-}$ is very similar to the CT induced anionic decompositions of other dioxetanones,[30,31,59] and its thermolysis and chemiexcitation can be also described by the GRCTIL mechanism. Meanwhile, similar results were found in the thermolysis of $\mathbf{III}^-$. (Figures S7 and S9) As Figure S6B shown, the energies of non-CT S_0 PEC (in the vicinities of reactant and product) is almost unaffected by DMSO, but the energies of CT region after TS is lower than that in gas phase.

No significant changes in key geometric structures and PECs of the $\mathbf{III}^{3-}$ decomposition were found, when the reaction field is altered from gas phase to DMSO. Hence, considering the compromise between chemical accuracy and computational cost, we performed the TSH simulation in gas phase to confirm the GRCTIL mechanism and provide the dynamics information for $\mathbf{III}^{3-}$ decomposition. First, the average distributions of O_a-O_b and C_2-C_3 at different time (Figure 8) clearly indicate a two-stage decay process. The fast O_a-O_b elongation takes place before 20 fs, while the C_2-C_3 distance does not change obviously until the O_a-O_b distance reached ∼2.5 Å. The further rupture of C_2-C_3 is observed after 40 fs. This indicates that the cleavages of O_a-O_b and C_2-C_3 are asynchronous, which is in line with the results in Figure 7C. Second, the evolution of average Mulliken charge population (Figure 9A) clearly displays the gradual CT from $\mathbf{IV}^{3-}$ to CO_2 (within ∼20 fs), and a gradual BCT from CO_2 to $\mathbf{IV}^{3-}$ (20−60 fs), which respectively match with the asynchronous cleavages of O_a-O_b (0−20 fs) and C_2-C_3 (>40 fs) (Figure 8) on the time scales and is also observed in Figure 7D. Finally, the transition stages of two electronic state were observed in the time evolution of average fractional occupations of S_0 and S_1 states (Figure 9B). In the first stage (stage 1), the average fractional occupation of S_1 increases from zero to approximately 0.7, implying the existence of a CI within 20 fs, where the obvious CT of $\mathbf{IV}^{3-} \rightarrow CO_2$ and the O_a-O_b bond rupture takes place at the same time. Then the average fractional occupation of S_1 state decreases to 0.4 and becomes stable after 70 fs implying another CI in stage 2. The exactly matched time scales of the O_a-O_b/C_2-C_3 bond cleavage and the CT of $\mathbf{IV}^{3-} \rightarrow CO_2$/BCT of $CO_2 \rightarrow \mathbf{IV}^{3-}$ is also consistent with above results in Figures 7C and 7D. Therefore, the two variation periods for S_1 population could be attributed to two successive nonadiabatic transitions governed

DOI: 10.1021/jacs.6b09119
J. Am. Chem. Soc. 2017, 139, 1106−1119

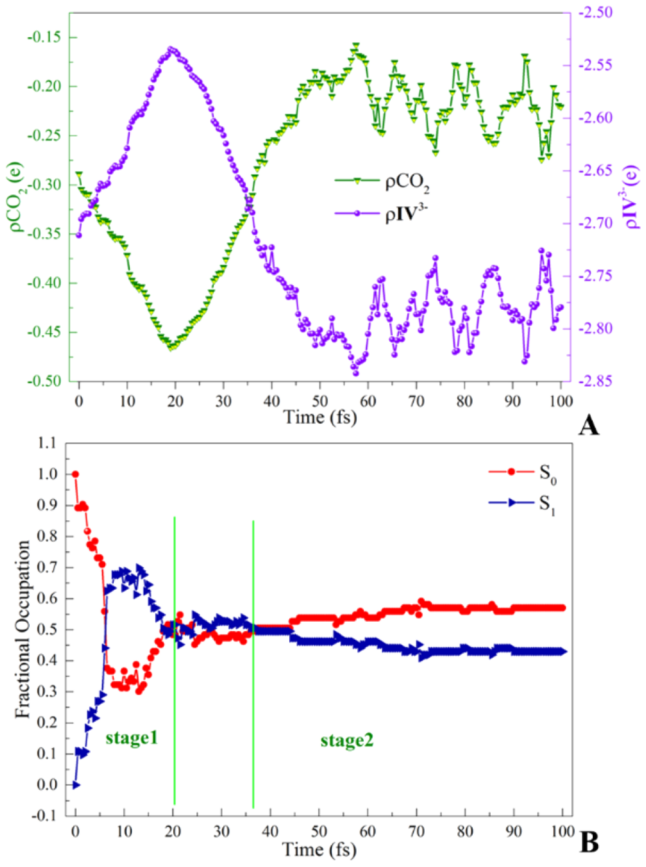

Figure 9. Time evolution of the average Mulliken charge population of $\mathbf{IV}^{3-}$ and CO_2 moieties (A), and the fractional occupations of the S_0 and S_1 states during the dynamics evolution of $\mathbf{III}^{3-}$ (B) (average over 100 trajectories) obtained by the TSH dynamics in gas phase at the SF-BHHLYP/6-31G(d,p) level.

by the two CIs. And two CIs in these two stages have been optimized by the SF-DFT method and correspond to the ruptures of O_a-C_b and C_2-C_3 bonds, respectively (see Figure S8 for the geometric information on the two CIs). The same results were found in the TSH simulation of $\mathbf{III}^-$ decomposition in gas phase (Figures S9–S11). Therefore, the results of TSH calculations and electronic structure computations support that the $\mathbf{III}^{3-}$ decomposition follows the GRCTIL mechanism, and accomplishes nonadiabatic transition through the two CIs to emit light.

In addition, the quantum yield of $\mathbf{IV}^{3-}$ of the S_1 state (Φs) from the chemiexcitation in the $\mathbf{III}^{3-}$ decomposition is also estimated according to the results of TSH simulation. For dioxetane-based CL or BL, Φs is the yield of electronic excited-state products (e.g., $\mathbf{IV}^{3-}$) formed during the decompositions of dioxetanones, i.e., the branch ratio of the S_0- and S_1-state after the nonadiabatic transition.[75] Φs and Φ_{FL} (the fluorescence yield, i.e., the quantum yield of radiative decay of the excited product) determine the CL or BL yield (Φ_{CL} or Φ_{BL}), that is $\Phi_{CL/BL} = \Phi_S \times \Phi_{FL}$. As shown in Figure 7B, at the end of TSH simulation (100 fs), $\mathbf{III}^{3-}$ nearly decomposes completely, and 57 and 43 trajectories were found on the S_0 and S_1 states, respectively. Thus, the branch ratio of S_1 and S_0 is estimated to 43% in the chemiluminescent decomposition of $\mathbf{III}^{3-}$ in gas phase, which is higher than that (34% in Figure S11B) in $\mathbf{III}^-$ decomposition and is consistent in magnitude with the value (64%) estimated based on Landau–Zener formula (see details in SI). Although there is no Φ_{FL} or Φ_{CL} of **IV** reported in experiments, the high Φ_S obtained by the TSH simulation suggests that the $\mathbf{III}^{3-}$ decomposition could contribute to the high efficiency of *W. scintillans* BL. Combining the thermochemical data and dynamics simulation results, we suggest that $\mathbf{III}^{3-}$ is more favorable and more efficient for *W. scintillans* BL.

4. CONCLUSION

The luciferin of deep-sea squid, *W. scintillans*, has a universal core skeleton (**ImPy**) in about eight phyla of bioluminescent organisms. The BL mechanism proposed by Tsuji has not been confirmed by any strong theoretical or experimental evidence. The biggest challenge is to elucidate the mechanisms of two key steps, oxygenation of luciferin (**I**) and the thermolysis of the peroxide intermediate (**III**). The oxygenation process is a general step in almost all oxygen-dependent BL systems. The thermolysis of the parent skeleton of **III**, dioxetanone, is the key step to produce light emitter for most BL and organic CL. In this paper, the two steps were systematically investigated by reliable electronic structure computations at the DFT and TDDFT level, and the nonadiabatic molecular dynamics simulation with SF-DFT. Both the computed ΔG_{SET} for the SET process and the estimated k_{ET} based on Marcus theory demonstrate that the SET process is responsible for the oxygenation of $\mathbf{I}^{3-}$. This SET process has been experimentally confirmed in the oxygenation of firefly luciferin. In DMSO, no matter whether $^1[\mathbf{I}^{\bullet 2-}\cdots O_2{}^{\bullet -}]$ or $^3[\mathbf{I}^{\bullet 2-}\cdots O_2{}^{\bullet -}]$ as the initial state, the C_2-oxygentation is more energetically feasible than the C_3-oxygentation. $^1[\mathbf{I}^{\bullet 2-}\cdots O_2{}^{\bullet -}]$ goes through four TSs to form $\mathbf{III}^{3-}$ via nucleophilic addition followed by a biradical annihilation after TS2, while $^3[\mathbf{I}^{\bullet 2-}\cdots O_2{}^{\bullet -}]$ needs a ISC process via a S/T surface intersection to produce $\mathbf{III}^{3-}$ in C_2-oxygentation. The decompositions of $\mathbf{III}^{2-}$ and $\mathbf{III}^{3-}$ follow by entropic trapping and GRCTIL mechanisms, respectively, which is similar to the simple dioxetanones. The decomposition of $\mathbf{III}^{3-}$ is energetically more feasible than $\mathbf{III}^{2-}$, $\mathbf{III}^-$, and **III**. The high quantum yield of $\mathbf{IV}^{3-}$ in the S_1 state (Φ_S = 43%) indirectly supports that the $\mathbf{III}^{3-}$decomposition is the step to produce light emitter of the *W. scintillans* BL. The SET-oxygenation and GRCTIL mechanism of *W. scintillans* BL in the current study could facilitate the understanding of most oxygen-dependent BL. The further study for the identification of light emitter of the *W. scintillans* BL is ongoing in our group.

■ ASSOCIATED CONTENT

Supporting Information

The Supporting Information is available free of charge on the ACS Publications website at DOI: 10.1021/jacs.6b09119.

The details for calculating the ΔG_{SET} and k_{ET} for the SET process between $\mathbf{I}^{3-}$ and $^3O_2$, and the estimation of Φ_S in $\mathbf{III}^{3-}$ decomposition based on Landau–Zener formula. The NOs used to represent the electronic states for $\mathbf{I}^{3-}$ oxygenation and $\mathbf{III}^{2-}/\mathbf{III}^{3-}$ decompositions; The S_0 PECs of the C_2- and C_3-oxygenation of $\mathbf{I}^-$ ($-OSO_3H$) in DMSO computed at the UCAM-B3LYP/6-31G(d,p) level. The S_0 PECs of the C_2- and C_3-oxygenation of $\mathbf{I}^{3-}$ in DMSO computed at the UCAM-B3LYP/6-31G(d,p) level with dispersion. The comparison of S_0 PECs of the $\mathbf{III}^{2-}/\mathbf{III}^{3-}$ ($-OSO_3^-$) decomposition in gas phase and DMSO calculated at the UCAM-B3LYP/6-31G(d,p) level; The S_0 and approximated diabatic PECs, and the

DOI: 10.1021/jacs.6b09119
J. Am. Chem. Soc. 2017, 139, 1106–1119

variation of the key geometric parameters and Mulliken charge population in **III**/**III**$^-$(−OSO_3H) decompositions calculated by (TD) UCAM-B3LYP/6-31G(d,p); The time evolution of detailed two-dimensional distribution of the C_2−C_3 and O_a−O_b bond distances, the average Mulliken charge populations of **IV**/**IV**$^-$(−OSO_3H) and CO_2 moieties, and the fractional occupation of S_0 and S_1 states obtained by TSH simulation at the SF-BHHLYP/6-31G(d,p) level; Cartesian coordinates for the RC, Int, and TS optimized at the (TD) CAM-B3LYP/6-31G(d,p) level, and CIs optimized at the SF-BHHLYP/6-31G(d,p) level. (PDF)

AUTHOR INFORMATION

Corresponding Author

*yajun.liu@bnu.edu.cn

ORCID

Ya-Jun Liu: 0000-0001-8761-5339

Notes

The authors declare no competing financial interest.

ACKNOWLEDGMENTS

This work was supported by grants from the National Natural Science Foundation of China (Grant Nos. Grants 21273021, 21325312, 21421003, and 21673020).

REFERENCES

(1) Bianchi, A.; Dufort, S.; Lux, F.; Fortin, P.-Y.; Tassali, N.; Tillement, O.; Coll, J.-L.; Crémillieux, Y. *Proc. Natl. Acad. Sci. U. S. A.* **2014**, *111*, 9247−9252.

(2) Schaub, F. X.; Reza, M. S.; Flaveny, C. A.; Li, W.; Musicant, A. M.; Hoxha, S.; Guo, M.; Cleveland, J. L.; Amelio, A. L. *Cancer Res.* **2015**, *75*, 5023−5033.

(3) Wang, F.; Wang, Z.; Hida, N.; Kiesewetter, D. O.; Ma, Y.; Yang, K.; Rong, P.; Liang, J.; Tian, J.; Niu, G.; Chen, X. *Proc. Natl. Acad. Sci. U. S. A.* **2014**, *111*, 5165−5170.

(4) Markova, S. V.; Vysotski, E. S. *Biochemistry (Moscow)* **2015**, *80*, 714−732.

(5) Purtov, K. V.; Petushkov, V. N.; Baranov, M. S.; Mineev, K. S.; Rodionova, N. S.; Kaskova, Z. M.; Tsarkova, A. S.; Petunin, A. I.; Bondar, V. S.; Rodicheva, E. K.; Medvedeva, S. E.; Oba, Y.; Oba, Y.; Arseniev, A. S.; Lukyanov, S.; Gitelson, J. I.; Yampolsky, I. V. *Angew. Chem., Int. Ed.* **2015**, *54*, 8124−8128.

(6) Dubinnyi, M. A.; Kaskova, Z. M.; Rodionova, N. S.; Baranov, M. S.; Gorokhovatsky, A. Y.; Kotlobay, A.; Solntsev, K. M.; Tsarkova, A. S.; Petushkov, V. N.; Yampolsky, I. V. *Angew. Chem., Int. Ed.* **2015**, *54*, 7065−7067.

(7) Haddock, S. H. D.; Moline, M. A.; Case, J. F. *Annu. Rev. Mar. Sci.* **2010**, *2*, 443−493.

(8) Widder, E. A. *Science* **2010**, *328*, 704−708.

(9) Tsuji, F. I. *Proc. Natl. Acad. Sci. U. S. A.* **1985**, *82*, 4629−4632.

(10) Tsuji, F. I. *Biochem. Biophys. Res. Commun.* **2005**, *338*, 250−253.

(11) Tsuji, F. I. *Biochim. Biophys. Acta, Biomembr.* **2002**, *1564*, 189−197.

(12) Hayashi, K.; Kawai, Y. L.; Yura, K.; Yoshida, M.-a.; Ogura, A.; Hata, K.; Nakabayashi, K.; Okamura, K. *Mitochondrial DNA* **2016**, 1−2.

(13) DeLoney-Marino, C. R.; Wolfe, A. J.; Visick, K. L. *Appl. Environ. Microbiol.* **2003**, *69*, 7527−7530.

(14) Yazzie, N.; Salazar, K. A.; Castillo, M. G. *Fish Shellfish Immunol.* **2015**, *44*, 342−355.

(15) Tong, D.; Rozas, N. S.; Oakley, T. H.; Mitchell, J.; Colley, N. J.; McFall-Ngai, M. J. *Proc. Natl. Acad. Sci. U. S. A.* **2009**, *106*, 9836−9841.

(16) Jones, B. W.; Nishiguchi, M. K. *Mar. Biol.* **2004**, *144*, 1151−1155.

(17) Dilly, P. N.; Herring, P. J. *J. Zool.* **1978**, *186*, 47−59.

(18) Tsuji, F. I.; Leisman, G. B. *Proc. Natl. Acad. Sci. U. S. A.* **1981**, *78*, 6719−6723.

(19) Fujii, T.; Ahn, J.-Y.; Kuse, M.; Mori, H.; Matsuda, T.; Isobe, M. *Biochem. Biophys. Res. Commun.* **2002**, *293*, 874−879.

(20) Chou, C.-M.; Tung, Y.-W.; Isobe, M. *Bioorg. Med. Chem.* **2014**, *22*, 4177−4188.

(21) Isobe, M.; Kuse, M.; Tani, N.; Fujii, T.; Matsuda, T. *Proc. Jpn. Acad., Ser. B* **2008**, *84*, 386−392.

(22) Kuse, M.; Isobe, M. *Tetrahedron* **2000**, *56*, 2629−2639.

(23) Kuse, M. *Biosci., Biotechnol., Biochem.* **2014**, *78*, 731−736.

(24) Goto, T.; Iio, H.; Inoue, S.; Kakoi, H. *Tetrahedron Lett.* **1974**, *15*, 2321−2324.

(25) Inoue, S.; Sugiura, S.; Kakoi, H.; Hasizume, K.; Goto, T.; Iio, H. *Chem. Lett.* **1975**, *4*, 141−144.

(26) Inoue, S.; Kakoi, H.; Goto, T. *Tetrahedron Lett.* **1976**, *17*, 2971−2974.

(27) Haddock, S. H. D.; Rivers, T. J.; Robison, B. H. *Proc. Natl. Acad. Sci. U. S. A.* **2001**, *98*, 11148−11151.

(28) Jiang, T.; Du, L.; Li, M. *Photochem. Photobiol. Sci.* **2016**, *15*, 466−480.

(29) Teranishi, K.; Shimomura, O. *Biochim. Biophys. Acta, Gen. Subj.* **2008**, *1780*, 784−792.

(30) Yue, L.; Liu, Y.-J.; Fang, W.-H. *J. Am. Chem. Soc.* **2012**, *134*, 11632−11639.

(31) Ding, B.-W.; Naumov, P.; Liu, Y.-J. *J. Chem. Theory Comput.* **2015**, *11*, 591−599.

(32) Chen, S.-F.; Ferré, N.; Liu, Y.-J. *Chem. - Eur. J.* **2013**, *19*, 8466−8472.

(33) Liu, Z.-J.; Stepanyuk, G. A.; Vysotski, E. S.; Lee, J.; Markova, S. V.; Malikova, N. P.; Wang, B.-C. *Proc. Natl. Acad. Sci. U. S. A.* **2006**, *103*, 2570−2575.

(34) Hou, C.; Liu, Y.-J.; Ferré, N.; Fang, W.-H. *Chem. - Eur. J.* **2014**, *20*, 7979−7986.

(35) McCapra, F.; Chang, Y. C. *Chem. Commun. (London)* **1967**, 1011−1012.

(36) McCapra, F. *Acc. Chem. Res.* **1976**, *9*, 201−208.

(37) Shimomura, O.; Johnson, F. H. *Biochem. Biophys. Res. Commun.* **1971**, *44*, 340−346.

(38) Kazuo Hori, M. J. C. *Proc. Natl. Acad. Sci. U.S.A.* **1973**, *70*, 4.

(39) Ohmiya, Y.; Hirano, T. *Chem. Biol.* **1996**, *3*, 337−347.

(40) Adamczyk, M.; Akireddy, S. R.; Johnson, D. D.; Mattingly, P. G.; Pan, Y.; Reddy, R. E. *Tetrahedron* **2003**, *59*, 8129−8142.

(41) Teranishi, K.; Ueda, K.; Nakao, H.; Hisamatsu, M.; Yamada, T. *Tetrahedron Lett.* **1994**, *35*, 8181−8184.

(42) Goto, T. *Pure Appl. Chem.* **1968**, *17*, 421−442.

(43) Nakamura, H.; Wu, C.; Inouye, S.; Murai, A. *J. Am. Chem. Soc.* **2001**, *123*, 1523−1524.

(44) Isobe, M.; Takahashi, H.; Usami, K.; Hattori, M.; Nishigohri, Y. *Pure Appl. Chem.* **1994**, *66*, 765.

(45) Ken Fujimori, S. H. N.; Katsuhisa, A.; Motohiro, M. *J. Chem. Soc. Perkin Trans. 2* **1993**, *2*, 5.

(46) Isobe, H.; Yamanaka, S.; Kuramitsu, S.; Yamaguchi, K. *J. Am. Chem. Soc.* **2008**, *130*, 132−149.

(47) Usami, K.; Isobe, M. *Tetrahedron* **1996**, *52*, 12061−12090.

(48) Head, J. F.; Inouye, S.; Teranishi, K.; Shimomura, O. *Nature* **2000**, *405*, 372−376.

(49) Kondo, H.; Igarashi, T.; Maki, S.; Niwa, H.; Ikeda, H.; Hirano, T. *Tetrahedron Lett.* **2005**, *46*, 7701−7704.

(50) Liu, Z.-J.; Stepanyuk, G. A.; Vysotski, E. S.; Lee, J.; Markova, S. V.; Malikova, N. P.; Wang, B.-C. *Proc. Natl. Acad. Sci. U. S. A.* **2006**, *103*, 2570−2575.

(51) Visitsatthawong, S.; Chenprakhon, P.; Chaiyen, P.; Surawatanawong, P. *J. Am. Chem. Soc.* **2015**, *137*, 9363−9374.

(52) Branchini, B. R.; Behney, C. E.; Southworth, T. L.; Fontaine, D. M.; Gulick, A. M.; Vinyard, D. J.; Brudvig, G. W. *J. Am. Chem. Soc.* **2015**, *137*, 7592−7595.

DOI: 10.1021/jacs.6b09119
J. Am. Chem. Soc. 2017, 139, 1106−1119

(53) Eremeeva, E. V.; Natashin, P. V.; Song, L.; Zhou, Y.; van Berkel, W. J. H.; Liu, Z.-J.; Vysotski, E. S. *ChemBioChem* **2013**, *14*, 739−745.
(54) Chen, S.-F.; Navizet, I.; Roca-Sanjuán, D.; Lindh, R.; Liu, Y.-J.; Ferré, N. *J. Chem. Theory Comput.* **2012**, *8*, 2796−2807.
(55) Chen, S.; Navizet, I.; Lindh, R.; Liu, Y.; Ferré, N. *J. Phys. Chem. B* **2014**, *118*, 2896−2903.
(56) Natashin, P. V.; Ding, W.; Eremeeva, E. V.; Markova, S. V.; Lee, J.; Vysotski, E. S.; Liu, Z.-J. *Acta Crystallogr., Sect. D: Biol. Crystallogr.* **2014**, *70*, 720−732.
(57) Yoshihiro, O.; Satoshi, K.; Mitsuhiro, N.; Haruki, N. *Bull. Chem. Soc. Jpn.* **2005**, *78*, 1197−1205.
(58) White, E. H.; Zafiriou, O.; Kagi, H. H.; Hill, J. H. M. *J. Am. Chem. Soc.* **1964**, *86*, 940−941.
(59) Yue, L.; Liu, Y.-J. *J. Chem. Theory Comput.* **2013**, *9*, 2300−2312.
(60) King, D. W.; Cooper, W. J.; Rusak, S. A.; Peake, B. M.; Kiddle, J. J.; O'Sullivan, D. W.; Melamed, M. L.; Morgan, C. R.; Theberge, S. M. *Anal. Chem.* **2007**, *79*, 4169−4176.
(61) Vico, L. D.; Liu, Y.-J.; Krogh, J. W.; Lindh, R. *J. Phys. Chem. A* **2007**, *111*, 8013−8019.
(62) Yue, L.; Roca-Sanjuán, D.; Lindh, R.; Ferré, N.; Liu, Y.-J. *J. Chem. Theory Comput.* **2012**, *8*, 4359−4363.
(63) Liu, F.; Liu, Y.-J.; Vico, L. D.; Lindh, R. *J. Am. Chem. Soc.* **2009**, *131*, 6181−6188.
(64) Liu, F.; Liu, Y.-J.; Vico, L. D.; Lindh, R. *Chem. Phys. Lett.* **2009**, *484*, 69−75.
(65) Yanai, T.; Tew, D. P.; Handy, N. C. *Chem. Phys. Lett.* **2004**, *393*, 51−57.
(66) Marcus, R. A. *Rev. Mod. Phys.* **1993**, *65*, 599.
(67) Krylov, A. I. *Chem. Phys. Lett.* **2001**, *338*, 375−384.
(68) Krylov, A. I.; Sherrill, C. D. *J. Chem. Phys.* **2002**, *116*, 3194−3203.
(69) Casanova, D.; Head-Gordon, M. *J. Chem. Phys.* **2008**, *129*, 064104.
(70) Hirata, S.; Head-Gordon, M. *Chem. Phys. Lett.* **1999**, *314*, 291−299.
(71) Huix-Rotllant, M.; Natarajan, B.; Ipatov, A.; Muhavini Wawire, C.; Deutsch, T.; Casida, M. E. *Phys. Chem. Chem. Phys.* **2010**, *12*, 12811−12825.
(72) Liu, F.; Gan, Z.; Shao, Y.; Hsu, C.-P.; Dreuw, A.; Head-Gordon, M.; Miller, B. T.; Brooks, B. R.; Yu, J.-G.; Furlani, T. R.; Kong, J. *Mol. Phys.* **2010**, *108*, 2791−2800.
(73) Harabuchi, Y.; Maeda, S.; Taketsugu, T.; Minezawa, N.; Morokuma, K. *J. Chem. Theory Comput.* **2013**, *9*, 4116−4123.
(74) Minezawa, N.; Gordon, M. S. *J. Phys. Chem. A* **2009**, *113*, 12749−12753.
(75) Yue, L.; Lan, Z.; Liu, Y.-J. *J. Phys. Chem. Lett.* **2015**, *6*, 540−548.
(76) Pittner, J.; Lischka, H.; Barbatti, M. *Chem. Phys.* **2009**, *356*, 147−152.
(77) Werner, U.; Mitrić, R.; Suzuki, T.; Bonačić-Koutecký, V. *Chem. Phys.* **2008**, *349*, 319−324.
(78) Verlet, L. *Phys. Rev.* **1967**, *159*, 98−103.
(79) Verlet, L. *Phys. Rev.* **1968**, *165*, 201−214.
(80) Swope, W. C.; Andersen, H. C.; Berens, P. H.; Wilson, K. R. *J. Chem. Phys.* **1982**, *76*, 637−649.
(81) Sellner, B.; Barbatti, M.; Lischka, H. *J. Chem. Phys.* **2009**, *131*, 024312.
(82) Liu, Y.-J.; Tian, Y.-C.; Fang, W.-H. *J. Chem. Phys.* **2010**, *132*, 014306.
(83) Landau, L. D. *Phys. Z. Sowjetunion* **1932**, *2*, 46−51.
(84) Zener, C. *Proc. R. Soc. London, Ser. A* **1932**, *137*, 696−702.
(85) Hehre, W. J.; Ditchfield, R.; Pople, J. A. *J. Chem. Phys.* **1972**, *56*, 2257−2261.
(86) Hariharan, P. C.; Pople, J. A. *Theoretical Chemistry Accounts: Theory, Computation, and Modeling (Theoretica Chimica Acta)* **1973**, *28*, 213−222.
(87) Frisch, M. J.; Trucks, G. W.; Schlegel, H. B.; Scuseria, G. E.; Robb, M. A.; Cheeseman, J. R.; Scalmani, G.; Barone, V.; Mennucci, B.; Petersson, G. A.; Nakatsuji, H.; Caricato, M.; Li, X.; Hratchian, H. P.; Izmaylov, A. F.; Bloino, J.; Zheng, G.; Sonnenberg, J. L.; Hada, M.; Ehara, M.; Toyota, K.; Fukuda, R.; Hasegawa, J.; Ishida, M.; Nakajima, T.; Honda, Y.; Kitao, O.; Nakai, H.; Vreven, T.; Montgomery, J. A., Jr.; Peralta, J. E.; Ogliaro, F.; Bearpark, M.; Heyd, J. J.; Brothers, E.; Kudin, K. N.; Staroverov, V. N.; Kobayashi, R.; Normand, J.; Raghavachari, K.; Rendell, A.; Burant, J. C.; Iyengar, S. S.; Tomasi, J.; Cossi, M.; Rega, N.; Millam, J. M.; Klene, M.; Knox, J. E.; Cross, J. B.; Bakken, V.; Adamo, C.; Jaramillo, J.; Gomperts, R.; Stratmann, R. E.; Yazyev, O.; Austin, A. J.; Cammi, R.; Pomelli, C.; Ochterski, J. W.; Martin, R. L.; Morokuma, K.; Zakrzewski, V. G.; Voth, G. A.; Salvador, P.; Dannenberg, J. J.; Dapprich, S.; Daniels, A. D.; Farkas, O.; Foresman, J. B.; Ortiz, J. V.; Cioslowski, J.; Fox, D. J. *Gaussian 09*, revision A.02; Gaussian, Inc.: Wallingford, CT, 2009.
(88) Barbatti, M.; Granucci, G.; Persico, M.; Ruckenbauer, M.; Vazdar, M.; Eckert-Maksić, M.; Lischka, H. *J. Photochem. Photobiol., A* **2007**, *190*, 228−240.
(89) Barbatti, M.; Granucci, G.; Ruckenbauer, M.; Pittner, J.; Persico, M.; Lischka, H. *NEWTON-X: A Package for Newtonian Dynamics Close to the Crossing Seam*, version 1.3; 2012; http://www.newtonx.org.
(90) Schmidt, M. W.; Baldridge, K. K.; Boatz, J. A.; Elbert, S. T.; Gordon, M. S.; Jensen, J. H.; Koseki, S.; Matsunaga, N.; Nguyen, K. A.; Su, S.; Windus, T. L.; Dupuis, M.; Montgomery, J. A. *J. Comput. Chem.* **1993**, *14*, 1347−1363.
(91) Noyes, R. M. *J. Am. Chem. Soc.* **1955**, *77*, 2042−2045.
(92) Noyes, R. M. *J. Am. Chem. Soc.* **1956**, *78*, 5486−5490.
(93) Winstein, S.; Clippinger, E.; Fainberg, A. H.; Robinson, G. C. *J. Am. Chem. Soc.* **1954**, *76*, 2597−2598.
(94) Kavarnos, G. J.; Turro, N. J. *Chem. Rev.* **1986**, *86*, 401−449.
(95) Werner, H. J.; Staerk, H.; Weller, A. *J. Chem. Phys.* **1978**, *68*, 2419−2426.
(96) Steiner, U. E.; Ulrich, T. *Chem. Rev.* **1989**, *89*, 51−147.
(97) El-Sayed, M. A. *J. Chem. Phys.* **1963**, *38*, 2834−2838.

DOI: 10.1021/jacs.6b09119
J. Am. Chem. Soc. 2017, 139, 1106−1119